Orbits and occultation opportunities of 15 TNOs observed by new horizons

Porter, Simon B.; Spencer, John R.; Verbiscer, Anne; Benecchi, Susan; Weaver, H. A.; Wen Lin, Hsing; Kavelaars, J. J.; Fraser, Wesley C.; Gerdes, David W.; Buie, Marc W.; Singer, Kelsi N.; Parker, Joel W.; Stern, S. Alan

Publisher's version / Version de l'éditeur:
https://doi.org/10.3847/PSJ/ac3491
The Planetary Science Journal, 3, 1, p. 23, 2022-01-01

The Planetary Science Journal, 3:23 (19pp), 2022 January https://doi.org/10.3847/PSJ/ac3491

Orbits and Occultation Opportunities of 15 TNOs Observed by New Horizons

Simon B. Porter[1], John R. Spencer[1], Anne Verbiscer[2], Susan Benecchi[3], H. A. Weaver[4], Hsing Wen Lin[5], J. J. Kavelaars[6], Wesley C. Fraser[6], David W. Gerdes[5,7], Marc W. Buie[1], Kelsi N. Singer[1], Joel W. Parker[1], and S. Alan Stern[1]
[1] Southwest Research Institute, 1050 Walnut Street, Suite 300, Boulder, CO 80302, USA; porter@boulder.swri.edu
[2] University of Virginia, P.O. Box 400325, Charlottesville, VA 22904, USA
[3] Planetary Science Institute, 1700 East Fort Lowell, Suite 106, Tucson, AZ 85719, USA
[4] Johns Hopkins University Applied Physics Laboratory, Laurel, MD, USA
[5] Department of Physics, University of Michigan, Ann Arbor, MI 48109, USA
[6] Herzberg Astronomy and Astrophysics Research Centre, National Research Council, 5071 West Saanich Road, Victoria, BC V9E 2E7, Canada
[7] Department of Astronomy, University of Michigan, Ann Arbor, MI 48109, USA
Received 2021 May 28; revised 2021 August 12; accepted 2021 August 30; published 2022 January 26

Abstract

We present high-precision orbits for 15 trans-Neptunian objects (TNOs) that have been observed by NASA's New Horizons spacecraft at distances from 0.092 to 2.2 au. We also give predictions of 66 future opportunities to observe stellar occultations by them in late 2021–2029, eight of which are possible to observe from the United States. Observation of these stellar occultations would allow searches for more contact-binary TNOs like the New Horizons flyby target (486958) Arrokoth. In addition, measuring the sizes and albedos of more TNOs helps to better calibrate models of the size–frequency distribution of the broader Kuiper Belt. The 15 TNOs we investigate are unique in that they have been observed by the New Horizons spacecraft, providing high-parallax observations that greatly help to restrict the uncertainty of their orbits. Our orbit determinations combine detailed analyses of observations from the Magellan, Subaru, and CTIO ground-based observatories; the Hubble Space Telescope; and the New Horizons spacecraft. They are referenced to the Gaia DR2 star catalog, while the occultation predictions use the latest Gaia EDR3 catalog for the occultation stars. Our analysis allows us to understand the uncertainties for all of our predicted occultation opportunities and thus the need for additional astrometry, if any, to observe these events and measure the sizes and shapes of small–midsize TNOs.

Unified Astronomy Thesaurus concepts: Orbit determination (1175); Stellar occultation (2135); Trans-Neptunian objects (1705); Resonant Kuiper belt objects (1396); Classical Kuiper belt objects (250)

Supporting material: figure set

1. Background and Motivation

Trans-Neptunian object (TNO) is a broad label for all natural bodies of the solar system that are beyond Neptune. Generally, this includes both objects that were formed at distances beyond the current orbital distance of Neptune at 30 au, commonly known as the "classical Kuiper Belt," and objects that were either scattered outward by Neptune's migration, dragged outward by mean-motion orbital resonances with Neptune, or both (Elliot et al. 2005). Most larger bodies and dwarf planets of the TNO population fall into the later category; e.g., Pluto is resonant with Neptune's orbit (Malhotra 1993), while Eris has been scattered into a highly excited orbit. The classical Kuiper Belt is characterized by orbits with low eccentricity, low inclination to Neptune's orbital plane, and semimajor axes between 39.4 and 47.7 au (Bannister et al. 2018). The best-characterized classical Kuiper Belt object (KBO) is (486958) Arrokoth (formerly 2014 MU_{69}), with a semimajor axis of 44.23 au, an eccentricity of 0.037, and an inclination of 2°.45 to the ecliptic plane (Porter et al. 2018), which the New Horizons spacecraft flew past on 2019 January 1.

NASA's New Horizons spacecraft launched on 2006 January 19 and flew past Jupiter on 2007 February 28 on the way to encountering its primary mission target, Pluto, on 2015 July 14. On 2016 July 1, NASA approved the New Horizons Kuiper Belt Extended Mission, enabling the New Horizons spacecraft to both have a close flyby with Arrokoth at a distance of 3538 km (Stern et al. 2019) and observe several other TNOs as it passed through the Kuiper Belt. Here we present the astrometric results for 15 of those TNOs observed by New Horizons. New Horizons observed these objects both at very close ranges (0.092–2.2 au) and at a broad range of Sun–target–observer phase angles (16°.6–122°). The combination of these two factors, along with Earth-based observations of the TNOs at phase angles of less than 2° (notably from the Hubble Space Telescope, HST, with high-precision astrometry), allows us to determine the orbits of these TNOs to much higher precision than is possible for most TNOs. These high-precision orbits allow us to predict future stellar occultation opportunities for these TNOs out to the end of the 2020s.

Of the 15 TNOs that we will discuss, 10 were discovered in the 2011–2012 ground-based search for a post-Pluto flyby target for New Horizons. None of them was close enough for New Horizons to reach with its limited fuel supply, but they were bright enough to target with the LOng Range Reconnaissance Imager (LORRI) camera (see below). These TNOs are 2011 HF_{103}, 2011 HJ_{103}, 2011 HK_{103}, 2011 HZ_{102}, 2011 JA_{32}, 2011 JW_{31}, 2011 JX_{31}, 2011 JY_{31}, 2012 HE_{85}, and (516977) 2012 HZ_{84}. The 2014 HST search for a post-Pluto flyby target for New Horizons produced three candidates: Arrokoth, 2014

OS_{393}, and 2014 PN_{70}. Arrokoth was chosen as the flyby target, but the spacecraft flew very close to 2014 OS_{393} and 2014 PN_{70} as well. Finally, three additional TNOs were discovered in 2018 that were close enough to the trajectory of New Horizons to enable LORRI observations of them. One object, 2004 LW_{31}, turned out to be a rediscovery of a previously lost TNO, while 2018 MF_{13} and 2018 MG_{13} were new discoveries. We were able to find occultation opportunities for all of these objects over the 2021–2029 time period.

Our primary motivation for predicting these occultation observations is to understand and place into context the extraordinary contact-binary shape of Arrokoth. It is a bilobate body with a larger lobe measuring approximately $20 \times 20 \times 10$ km and a smaller lobe of $15 \times 14 \times 10$ km, connected by a very thin neck (Spencer et al. 2020). Arrokoth's contact-binary nature was first determined by a stellar occultation and then confirmed with resolved New Horizons images (Stern et al. 2019; Buie et al. 2020). Because the Kuiper Belt is a population of objects that have been mostly isolated since they first formed from the protoplanetary disk (Levison et al. 2008; Nesvorný et al. 2010), small TNO shapes must illustrate fundamental accretionary processes. The contact-binary shape of Arrokoth is most likely primordial and intrinsic to its formation (Stern et al. 2019; McKinnon et al. 2020). In particular, McKinnon et al. (2020) showed that the weak neck of Arrokoth (the connection between the two lobes) did not have the strength to survive a collision at or above the escape velocity of the two lobes. They therefore must have come into contact while on a bound orbit with a decaying semimajor axis. This result implies that many other tight binaries in the early Kuiper Belt (and indeed across the early solar system) may have formed contact binaries in a similar manner. Planetesimal formation models generally produce large numbers of separated binaries (Nesvorný et al. 2010; Nesvorný & Vokrouhlický 2019), many of which would be tight enough to form contact binaries through solar nebula drag. This result is further supported by the large numbers of widely separated binaries that have been discovered in resolved HST and ground-based images (Grundy et al. 2019; Benecchi et al. 2020), implying an even larger fraction of tighter and contact binaries in the Kuiper Belt. Indeed, two of our targets (2011 JY_{31} and 2014 OS_{393}) have been observed to be close binaries (separations less than 200 km) based on resolved New Horizons observations (Weaver et al. 2021), despite appearing as single objects in prior HST Wide Field Camera 3 (WFC3) observations.

Stellar occultations occur when a solar system body passes in front of a star, causing that star to appear to blink out from particular locations on Earth. Currently, the best way to study the size and shape of TNOs is with stellar occultations. No existing or planned telescope, either on Earth or in space, can resolve the shape of small TNOs. However, stellar occultations of TNOs can and have probed the shape and size of large TNOs (e.g., Elliot et al. 2010; Sicardy et al. 2011; Ortiz et al. 2012, 2017). The advent of Gaia Data Release 2 (DR2)/Early Data Release 3 (EDR3) star positions has enabled occultation predictions of much smaller TNOs than ever attempted before. Prior to Gaia, the contribution of star uncertainty to occultation ground-track uncertainty was often hundreds of kilometers, making small TNO occultation observations impossible. Gaia EDR3 (Lindegren et al. 2020) provides star positional knowledge to a precision of a few milliarcseconds per occultation star, equating to a few kilometers of uncertainty in the ground track of an occultation. Arrokoth is the only small TNO that has been observed with a high-cadence occultation campaign, which revealed its contact-binary shape (Buie et al. 2020). But this powerful technique can and should be extended to determine the nature and origin of other small TNOs. Occultation predictions require extremely precise knowledge of the positions of both the TNO and star. We thus devote much of this work to describing our process for determining the astrometric positions of the TNOs in ground-based, HST, and New Horizons images and how we translate that into orbits and occultation predictions with estimated uncertainties. The combination of ground-based, HST, and New Horizons astrometry provides a parallax measurement of the moving sources, thereby reducing the uncertainty of the predicted tracks down to as low as a few tens of kilometers, enabling future occultation campaigns. The New Horizons data set is unique to these objects and makes them the best small–midsize TNO occultation targets.

Our secondary motivation for predicting these TNO occultations is to help calibrate the size–frequency distribution (SFD) of the Kuiper Belt. Occultation observations are one of the few ways in which the SFD of TNOs can be determined. The surveys from which TNOs are discovered are also used to measure the intrinsic TNO absolute magnitude distribution. From this, with albedo knowledge, the intrinsic size distribution can be inferred (Fraser et al. 2014). The predominant source of TNO albedo measurements comes from radiometry (e.g., Santos-Sanz et al. 2012; Fraser et al. 2014), which informs us of a target's geometric albedo, when combined with visible-light photometry and assumptions about the shape of the object. Converting the wealth of TNOs that the Vera Rubin Observatory is expected to discover (Vera C. Rubin Observatory LSST Solar System Science Collaboration et al. 2020) into an SFD will require such assumptions. As irregularly shaped and contact-binary TNOs appear to be quite common (e.g., Thirouin & Sheppard 2018, 2019), current albedo measurements have become suspect. We expect the smallest bodies to have the largest deviations away from spherical and therefore the most need of shape information. In addition, occultations can detect very tight binaries (Leiva et al. 2020); understanding how common tight binaries are in the Kuiper Belt is crucial to understanding its SFD.

The most thorough attempt to calibrate the SFD/albedo relationship of the Kuiper Belt was with thermal IR measurements using the Herschel Space Telescope 60–210 μm observations, able to measure TNO sizes down to about 110 km (Santos-Sanz et al. 2012), and were consistent with a 5% albedo for most scattered TNOs (Santos-Sanz et al. 2012). However, the number of objects that Herschel was able to observe was very limited (139 total), and Herschel is no longer operational. These estimates had to make assumptions about the shape, thermal emissivity, and rotation of the objects. The James Webb Space Telescope's MIRI observes shorter than the thermal peak of TNOs, and the Atacama Large Millimeter/submillimeter Array (ALMA) observes longer, so repeating this observation (even with a combination of MIRI and ALMA) is very difficult and could only be performed on significantly brighter objects than were targeted by Herschel. The only resolved measurement of the albedo of a subdwarf planet TNO is through analyses of the NH imagery of Arrokoth, which found that it has a Bond albedo of ≈6% and a geometric albedo of ≈21% (Hofgartner et al. 2021). The complicated shape of

Arrokoth thus plays a huge role in determining its brightness from the Earth, and that is undoubtedly true for other TNOs. Unlike thermal IR measurements, size and shape measurements of TNOs with occultations can account for shape effects and produce more accurate estimates of the true geometric albedos of TNOs and therefore help us understand the true current SFD of the Kuiper Belt.

Here we present our astrometric analysis of ground-based, HST, and New Horizons data, both in registering the images to Gaia DR2 stars and in measuring the positions of the TNOs in those images. We then present our high-precision, uncertainty-driven orbit determination procedure and how we use it to derive occultation predictions with well-defined uncertainty estimates. Finally, we present our predictions for what we think are the best occultation observation opportunities for these objects in both the United States and internationally in 2021–2029.

2. Astrometric Data and Analysis

2.1. Magellan MegaCam and IMACS Data

The oldest ground-based data reprocessed in this analysis were obtained in 2011, 2012, 2013, and 2014 with the Megacam camera (McLeod et al. 2015) on the Magellan Clay telescope. Megacam is a wide-field imager with 36 CCDs covering a 24 arcmin^2 field of view (McLeod et al. 2015), and the Magellan Clay telescope is a 6.5 m telescope operated by the Magellan Consortium at Las Campanas Observatory in Chile. The 2011 and 2012 Megacam observations used a standard "r" filter, while the 2013 and 2014 observations used a special, wider "gr" filter that covered both the g and r bands. In addition, the same field was observed in 2011 and 2012 with the Inamori-Magellan Areal Camera and Spectrograph (IMACS) Long Camera (Bigelow et al. 1998), also on Magellan Clay. The IMACS is a wide-field, multipurpose imaging spectrograph with an eight-CCD array covering a half-degree field of view (Bigelow et al. 1998). All of the IMACS observations used the "WB4800-7800" wideband filter. These were two of the early data sets used to search for post-Pluto targets for New Horizons and the first data set that was used to discover a significant number of TNOs in the vicinity of the New Horizons trajectory. These data sets were used to discover 10 of the 15 objects in this paper, 2011 HF_{103}, 2011 HJ_{103}, 2011 HK_{103}, 2011 HZ_{102}, 2011 JA_{32}, 2011 JW_{31}, 2011 JX_{31}, 2011 JY_{31}, 2012 HE_{85}, and 2012 HZ_{84}. In addition, we were able to find precoveries of 2014 OS_{393} and 2014 PN_{70} in the 2013 and 2014 Megacam images.

To obtain the best-quality absolute astrometry for these objects, we reprocessed all of this data set with Gaia DR2 (Gaia Collaboration et al. 2018). For the Megacam images, we began by building a database of the rough pointing of each of the 36 CCDs for each of the 3107 Megacam exposures. This allowed us to rapidly determine both which chips had a particular TNO on them and which of the images would be appropriate to create an empirical star background model. This latter step is especially important, as the background star density of these fields was extremely high, particularly in 2011 and 2012, when the field was especially close to the galactic plane. Once we knew which chips per exposure were needed, we could then produce World Coordinate System (WCS; Calabretta & Greisen 2002; Greisen & Calabretta 2002) corrections for only the needed images. To do this, we matched the stars in each needed CCD of each exposure with Gaia DR2 stars and calculated a correction for CRVAL1 and CRVAL2 (i.e., the R.A./decl. pointing of the image) and a rotational offset that was applied to the CD matrix. We used the Gaia DR2 catalog to find all of the stars in the image that were brighter than $G = 20.5$ and had low uncertainty in their proper motions (<1 mas yr^{-1}) and then corrected their locations for their proper motion and parallax. For each of the $\approx$30–2000 stars (depending on the field) per chip, we used the old Megacam pipeline WCS to mask out the area away from the star and calculate a rough centroid for each star. We then used the centroids to calculate a roughly mean pixel offset and discarded any centroids that did not roughly match that offset (blended stars were typical in these very dense fields). Finally, we used the good stars to estimate a best-fit pixel offset and rotation and save the resulting image with a corrected WCS. The star-centroid rms residuals for most images after correction were $\approx$0.1–0.2 pixels ($\approx$8–16 mas). Typically, the WCS offsets were only a few pixels, but when combining hundreds of images for star backgrounds, these offsets dramatically improved the quality of the star subtraction. For the 1435 IMACS images (with eight chips each), the procedure was generally similar, but since the IMACS images did not come with initial WCS solutions, we first initialized them with a local version of *astrometry.net* (Lang et al. 2010) before applying final Gaia DR2 corrections as before with the Megacam images.

To extract the TNOs from the Megacam and IMACS data, we first went object-by-object and found the location of the TNO on all chips for each night of data. If the object was not on any of the chips, that night was skipped. If the TNO was on an illuminated CCD, we used the Gaia-fit WCS to reproject the image to a 20×20 pixel window centered on the predicted location of the TNO, dividing by the exposure time. For each of these images, we next used the Gaia stars to extract windows of the same size centered on the 20 brightest stars in the field dimmer than $G = 16$, corrected for brightness with the Gaia G magnitude, and stacked them to produce an empirical model point-spread function (PSF). We next defined a "star WCS" that covered the sky background of the images that contained the TNO, reprojected images that did not contain the TNO to that frame, and stacked them to produce an empirical model star field. However, these were ground-based images with a PSF that varied over time due to atmospheric conditions. We therefore adapted the "Optimal Image Subtraction" method of Alard & Lupton (1998), using their method to find the optimal transformation between the measured PSF of the individual images and the PSF of the star model image and then applying that transformation to the model star background to produce a degraded model star field that more closely matched the images. Since the background stacks generally contained far more images than the object stacks, this procedure worked well. A disadvantage of this method is that it leaves some "ringing" on the margins of the images as a result of the convolution; we addressed that by increasing the size of the star WCS. We then reprojected the PSF-matched backgrounds to the same frame as the windows with the objects and subtracted the star model from the data. We then stacked together the sequential subtracted images; because of observing conditions, the number of images in a sequence varied from one to 160. If there were less than 10 images in a sequence, we discarded it, as the signal-to-noise ratio (S/N) of the TNO was likely too low to be useful. For the stacks of more than 10 images, we saved the sigma-clipped robust median of the images, as we found it most robust to the remaining star residuals after

subtraction. We also stacked and saved the individual PSFs of the images in the same way to provide a model PSF of the stack.

Once the automatic process above was complete, we performed visual vetting of the stacks. This provided the dual purpose of verifying that an object was visible in the stack and allowing a human to click on the rough pixel location of the TNO. Stacks where the TNO was not clearly visible, typically due to sky opacity or a saturated (and therefore not subtractable) star, were discarded. We then performed astrometry of the TNOs in the vetted stacks. We first fit a model PSF to the empirical PSF using the *astropy* (Astropy Collaboration et al. 2013) Gaussian 2D function. While a bivariate Gaussian normal distribution was not a perfect fit to the shape of the PSF, it was very close and allowed for the PSF to be nonsymmetrical, as was sometimes the case. We then used the Gaussian model and the human mouse click of the location of the object as a starting point and produced a best fit for the flux and x/y location of the object using the *SciPy* (Virtanen et al. 2020) "fmin" implementation of the Nelder & Mead (1965) downhill simplex optimizer. We used this best fit to seed a Markov Chain Monte Carlo (MCMC) uncertainty estimation using the *emcee* package (Foreman-Mackey et al. 2013). The output of *emcee* was a 3000-element discretely sampled probability distribution function (PDF) of the joint probabilities for the x/y pixel position and DN/s flux of the TNO. We then used the WCS of the image to convert the pixel positions of the cloud to R.A. and decl. and the photometric zero-point measured from the stars to convert the DN/s flux into astronomical magnitude. Because the images were registered to Gaia DR2 stars, and Gaia DR2 was registered to the International Celestial Reference Frame (ICRF; Ma et al. 1998, 2009), our final astrometry was effectively in the ICRF. Since the R.A. and decl. were generally well described by a bivariate normal distribution, we calculated and saved the R.A./decl. mean and covariance matrix and the mean and standard deviation of the magnitude. Because we were processing stacks of images that were shift-stacked at a given rate, we wanted to preserve that shift rate in the astrometry. We thus used the pixel location PDF to generate R.A./decl. clouds for the first, middle, and last images of the stack, resulting in three astrometric points per image stack.

2.2. Subaru Hyper Suprime-Cam Data

The highest-quality ground-based images used in this analysis were obtained in 2014, 2016, 2017, and 2020 with the Hyper Suprime-Cam (HSC; Miyazaki et al. 2012) wide-field imager mounted on the Subaru Telescope. The HSC is a prime-focus camera with a mosaic of 104 science CCDs covering a $1\overset{\circ}{.}5$ field of view with a pixel scale of 170 mas (Miyazaki et al. 2012). The Subaru Telescope is a 8.2 m telescope located on the summit of Maunakea, Hawaii, and is operated by the National Astronomical Observatory of Japan. The 2014 HSC observations (Proposal o14215) were conducted as a ground-based backup to the HST search described below. Since the HST search was successful, the 2014 data set was not used to search for new objects but did provide an excellent quality data set for recoveries and precoveries of TNOs discovered in other programs, particularly as most images had <500 mas seeing. The 2016 and 2017 observations (Proposals o16204 and o17203) were performed to extend and improve the orbits of TNOs that had been discovered in the Magellan campaigns and were potential long-range observation targets for New Horizons. The image quality in the 2016 and 2017 observations was not as great as in 2014 but was sufficient to recover all of the targeted TNOs. The 2020 HSC observations were performed as a new search for fresh TNOs for New Horizons to observe in 2020 and beyond. This search and its results will be discussed in a forthcoming paper. Since this search was looking for new TNOs, it was not optimized for recoveries of the already-known TNOs. However, we were able to recover four of our 15 objects in the 2020 images, extending some of them to a 9 yr arc. The 2014 and 2016 observations were performed with the HSC-R filter, while the 2017 and 2020 observations were performed with the similar but not identical HSC-R2 filter that replaced it. With the exception of a few test images, all of the HSC data considered here were obtained with 90 s exposures to minimize streaking of the apparent PSF of the TNOs. During the HSC observations, the telescope was fixed on the stars. Thus, a TNO would slowly move across a CCD over the course of a night (effectively dithering), while the stars stayed fixed, making for easier background subtraction. For the 2014 and 2016 observations, only a single field was used. For the 2017 observations, two slightly overlapping fields were used to increase coverage, with the telescope slewing to alternate between them. For the 2020 search, two slightly overlapping fields were used again, though with only one field per night. The four TNOs we recovered in those data were all in the 2020 field that was more optimized for objects that were closer to the Sun.

The first step in processing the HSC data was to process it though either the HSC or LSST pipeline,[8] where the HSC pipeline is a special-purpose fork of the LSST pipeline. In either case, these pipelines were used to apply dark frames, bias frames, and flat fields, as well as to fit the WCS of the images. We used the HSC pipeline to process the 2014, 2016, and 2017 data, along with custom *astrometry.net* format star catalogs derived from Gaia DR2. We used the LSST pipeline to process the 2020 data, along with the default Pan-STARRS star catalog (Magnier et al. 2013). The Pan-STARRS catalog has offsets from the Gaia DR2 star catalog but was self-consistent within a given night. This allowed us to calculate a mean astrometric offset for each night and apply it to the HSC data before further analysis. The offset was calculated by extracting an empirical star PSF (as described above) using the Gaia DR2 star positions, measuring the offset of the center of the star from the center of the nominal PSF, and averaging the offsets for the entire night. We also calculated these offsets for the 2014–2017 data, just to verify that they were near zero. Measuring the PSFs of the images also allowed us to determine the atmospheric extinction and seeing for each observation time during the nights. We used this to estimate an etendue as $\tau/\sqrt{\mathrm{FWHM_{AS}}}$, where τ is the atmospheric transparency and $\mathrm{FWHM_{AS}}$ is the FWHM of the PSF in arcseconds. We then coregistered all of the images for a given CCD per night to a mean pointing; since the roll angle was very consistent, we could do this by simply shifting the images, without doing a full reprojection. We used the best 33% of the images (as defined by their etendue) to create a background model for each CCD per night. We then used a similar optimal image subtraction (Alard & Lupton 1998) technique as for the Megacam data to create PSF-fit background models for all of

[8] https://pipelines.lsst.io/

the HSC data and subtracted them from the coregistered versions of the images.

To extract a TNO from the HSC data, we started by finding its location in all images. Initially, we did this with the mean orbit for the object using *spiceypy* (Annex et al. 2020a). Later, we used the orbit PDF (see below) to generate an estimate of the R.A., decl., and covariance for each time that the HSC image was obtained. We could then find which, if any, CCDs the TNO was on at that observation time and therefore generate a list of nights to process. For each night, we started by finding the maximum extent of a 3σ uncertainty cloud for the TNO. We could then define a reduction frame and WCS that contained at least the 3σ (and thus 99.5% probability) region but was no smaller than 21×21 pixels. Since the CCDs were roughly aligned either north–south or east–west, and the major uncertainty for most TNOs was east–west (due to uncertainty in their rate of motion), this resulted in images that were long strips for high-uncertainty TNOs and small squares for low-uncertainty TNOs. We then reprojected the coregistered, star-subtracted images to the reduction WCS, applying the measured Gaia DR2 offset. For our analysis, we used either all of the images with an etendue larger than 1.0 or the 66% of the images with the highest etendue, whichever was larger. This filtering did not degrade the images on very good nights and ensured that the worst images in the poor-seeing nights did not overly influence the final stacks. As for the Magellan data, we then visually inspected each nightly stack to ensure that the TNO was visible and manually selected its rough location. The latter was even more important for HSC, as we could recover objects that had large uncertainties and could be far from the center of the initial reduction WCS. We then fit the location of the TNO in the same way as for the Magellan data. The major difference was that for large images (i.e., larger than the minimum 21×21 pixels), we only performed a rough, 30-iteration estimate of the uncertainty with *emcee*. This was used to generate an interim orbit solution with lower uncertainties, and then the procedure was rerun. Like the Magellan data, this pixel location PSF was used to generate absolute ICRF astrometry for the first, middle, and last images of the night.

2.3. DECam Data

The Dark Energy Camera (DECam) images used in this analysis were obtained in 2018 June while searching for additional 2019 LORRI targets. The DECam (Flaugher et al. 2015) is a 3 deg^2 prime-focus camera mounted on the 4 m Blanco telescope at Cerro Tololo Inter-American Observatory in Chile. The focal plane consists of 62 $2k \times 4k$ fully depleted, red-sensitive CCDs. The 3 nights of observations were made with the "VR" filter, which has high transmission between 500 and 750 nm. Each data point consists of a coaddition of three 5 minute exposures. This data set was used to discover/recover three New Horizons targets: 2018 MF_{13}, 2018 MG_{13}, and the lost 2004 LW_{31}.

The DECam images were preprocessed by the DECam Community Pipeline (Valdes & Gruendl 2014). We resolved the astrometry against the Gaia DR2 star catalog (Gaia Collaboration et al. 2018) to have the same reference point and achieve the same level of accuracy with our other data sets. To search the TNOs in the high star density fields, we used the High Order Transform of PSF ANd Template Subtraction (HOTPANTS) package (Becker 2015), which is an implementation of the Alard & Lupton (1998) algorithm, to generate the differential images. The templates were created by median stacking the top 50% of better-seeing images of the fields. After the image subtractions, we linked the transient detections to be pair or triplet detections by assuming the TNO has a linear motion with a constant speed within a night. We claimed the discoveries once the pairs and triplets were linked with the other pairs or triplets on the other nights.

We follow up the discoveries with the Magellan Baade telescope with IMACS in 2019 June and July. The follow-up images were reduced by the standard procedure, consisting of bias subtraction and flat-field correction, and solving the WCS solution with the Gaia DR2 star catalog. The object search procedure is similar to the DECam TNO search we describe above.

Once the TNOs were retrieved and linked with the DECam detections from the follow-up images, we searched the possible prediscovery images from the achieved data using the Solar System Object Search at the Canadian Astronomy Data Centre (Gwyn et al. 2012). Object 2018 MF_{13} was found in six DECam images obtained in 2015 and then was able to link back to four CFHT/MegaCam images in 2004. Object 2018 MG_{13} was only able to link back to three 2017 detections with this procedure. One of the TNOs was able to link with the detections in our 2011 HSC images, and by using astrometry from the Minor Planet Center we identified this object as 2004 LW_{31} with large fitting residuals, which was discovered by Subaru/Suprime-Cam in 2004 and never observed after 2005. After retrieving the discovery images and resolving the astrometry with the Gaia DR2 star catalog, we confirmed that the object is the lost 2004 LW_{31}.

2.4. HST Data

Nine of our 15 TNOs were also observed with the HST/WFC3 (Kimble et al. 2008) UVIS channel prior to their observation by New Horizons. The HST is a 2.4 m telescope in low Earth orbit operated by the Space Telescope Science Institute (STScI) under contract with NASA. The WFC3 is a UVIS/IR imager that was installed on HST during the final shuttle serving mission in 2009. The UVIS channel on WFC3 consists of two CCDs covering a $164'' \times 164''$ field of view (Kimble et al. 2008). New Horizons team members led four HST programs to observe these TNOs to provide high-quality astrometry, as well as color measurement checks for binarity. Program GO-12535 (PI: Benecchi) was used to observe 2011 HZ_{102} (two orbits; listed as "VNH0010"), 2011 JW_{31} (two orbits; listed as "VNH0007"), and 2011 JY_{31} (two orbits; listed as "VNH0008") in 2012. The GO-12535 observations had four full-frame images per orbit, two each in F606W and F814W. Program GO-13633 (PI: Spencer) was the large, 194-orbit program that discovered Arrokoth (formerly 2014 MU_{69}), as well as 2014 OS_{393} (eight orbits; listed as "KBO1-R13C5," "KBO-TOO4-E31007AI," and "KBO-E31007AI-OCT14") and 2014 PN_{70} (six orbits; listed as "KBO1-R16C1" and "KBO-TOO5-G12000JZ"). The GO-13633 observations had five full-frame images per orbit, all with the very wide F350LP filter. Program GO-14092 (PI: Benecchi) in 2016 observed 2011 HK_{103} (two orbits), 2011 JW_{31} (two orbits), 2012 HE_{85} (two orbits), 2014 OS_{393} (four orbits), and 2014 PN_{70} (four orbits). The GO-14092 observations had five full-frame images per orbit, two in the F606W filter and three in the F814W filter. Program GO-15108 (PI: Kavelaars) observed 2014 OS_{393} (two orbits) and 2014 PN_{70} (two orbits) in 2018, with five full-frame

observations per orbit in the F350LP filter. In addition, 2011 JX_{31} was observed in one orbit of program GO-13716 in 2015 (PI: Trilling). The GO-13716 2011 JX_{31} observation consisted of eight images with the "UVIS2-C512C-SUB" subframe, four each in the F606W and F814W filters. The majority of these observations were obtained with the full frame of both UVIS chips so that the stars in the field could be used to produce high-quality astrometry. While the GO-13716 2011 JX_{31} observations were subframed, the star density was still high enough that we were able to use the same star fitting technique on them. The color results of these observations have been published in Benecchi et al. (2019), so here we only describe the orbit determination and occultation search.

Our analysis of the HST/WFC3 images was generally similar to (and based upon) the work described in Porter et al. (2018) to determine the orbit of Arrokoth. As with that analysis, we used the nondrizzled images to maximize the signal of faint targets. However, since that work, STScI has introduced the "flc" format images, which are generally similar to the "flt" images we used before but with superior charge transfer efficiency corrections. All of the analyses we present here used the flc format images as a starting point. We started by downloading the Gaia DR2 stars (Gaia Collaboration et al. 2018) in the field of view for each image. We then found the appropriate *Tiny Tim* model PSF (Krist et al. 2011) for each of the filters and CCDs used. Because the HST observations are tracked on the TNO, and the angular resolution of WFC3/UVIS is so high (pixel scale ≈40 mas), the stars in our HST images look streaked with the compound of the sky motion of the TNO and the motion of HST's orbit around the Earth. We thus used our knowledge of the orbital trajectory of HST, the orbit of the TNO that was used to guide the observation, and the *spiceypy* package (Annex et al. 2020a) to calculate the way in which the stars in each image would be smeared. We saved this as a "smear kernel," which found the R.A./decl. location of the TNO for 100 points during the exposure; since most exposures were 370 s, this was typically every 3.7 s. These locations could then be converted to pixel locations using the WFC3 WCS and then subtracted by the pixel location of the TNO at the observation mid-time. The resulting 100 pixel offsets were then used to shift the *Tiny Tim* PSF 100 times, and the mean of the 100 shifts was taken to produce a model smeared PSF. Next, we applied the appropriate proper-motion and parallax correction to the Gaia DR2 stars, extracted a small window around the expected location of the star with the flc WCS, and fit the smeared PSF to the star in the window. Since the smeared PSF was generally a different shape than any cosmic rays, this generally worked well. We then took all of the offsets from these fits, rejected the outliers, and used them to produce an initial WCS offset. We then repeated the star fitting procedure with that offset (so that the stars were roughly centered in the windows), this time using the best fits and *emcee* (Foreman-Mackey et al. 2013) to find the positional uncertainty of each star in the field. Since the shape of the streaked stars could be long and narrow, this often produced highly correlated x/y uncertainties for the stars. The number of stars used in this analysis varied by field but was typically between 30 and 300. Finally, we used the star PSFs and *emcee* to estimate the overall WCS solution and uncertainty. Since the roll angle of the HST images is very well determined, this ultimately consisted of offsets for CRVAL1 and CRVAL2 in the WCS headers of the images and a covariance matrix of the uncertainty in those offsets. The uncertainty in the WCS offset cloud was typically 5–10 mas, or a small fraction of the 40 mas WFC3/UVIS pixel size.

We processed the WFC3 images by first grouping them by filter in a given orbit; thus, the orbits with just F350LP images were processed together, and the orbits that split images between F606W and F814W had two reductions per orbit. We started by extracting windows centered on the predicted position of the TNO, stacking all windows in the filter–orbit set together, and fitting a *Tiny Tim* PSF to the stacked image. This best fit of the stack was used as the initial conditions for then fitting the individual windows, requiring their fits to be close to the stack solution in both pixel position and flux. This two-step process was particularly useful for the dimmer objects (i.e., 2014 OS_{393} and 2014 PN_{70}) that were not always apparent in the individual images but easily found in the stacks. We then used the best fit for the individual windows to fit x/y and flux PDFs for each image using *emcee*. We converted the x/y cloud into an R.A./decl. cloud (which included the offset because that was applied at the start) and then convolved them with the WCS offset uncertainty cloud to produce a full R.A./decl. uncertainty cloud. The flux PDF cloud was converted to magnitudes using the PHOTFLAM and PHOTPLAM header keywords, and an aperture correction was applied because of the small size of the windows. The final R.A./decl. and magnitude clouds were saved in the same format as used for the ground-based data. Because of WFC3's exceptional angular resolution, we did not need to subtract the background stars from these images. There were a few (<5%) images that we later dropped because they were photometric or astrometric outliers due to background stars.

2.5. New Horizons LORRI 4 × 4 Image Data

The New Horizons LORRI is the narrow-field optical camera on the New Horizons spacecraft (Cheng et al. 2008; Weaver et al. 2020). It is the primary instrument on New Horizons for observing distant targets, including dwarf planets and small-to-medium sized TNOs (Porter et al. 2016; Verbiscer et al. 2019). LORRI's optical assembly consists of a Ritchey–Chrétien telescope with a 20.8 cm diameter primary mirror, a focal length of 263 cm (F/12.6), and a three lens field-flattening assembly (Cheng et al. 2008; Weaver et al. 2020). It has no filters (so as to maximize throughput) and uses a back-illuminated CCD sensor with a 1024 × 1024 illuminated region (Cheng et al. 2008; Weaver et al. 2020). The angular resolution of LORRI is $1\farcs04$ pixel^{-1}, with a typical FWHM of 1.9 × 2.5 pixels (Cheng et al. 2008; Weaver et al. 2020). Because LORRI is fixed to the spacecraft and the New Horizons spacecraft does not have reaction wheels, all pointing of LORRI must be performed with the onboard thrusters. This means that exposures longer than a few seconds can only have a guaranteed pointing stability of within $3\farcs5$ without excessive propellant usage. Thus, most distant TNO observations were binned 4 × 4 on board the spacecraft, also reducing their downlink volume for minimal reduction in useful resolution. The exceptions were the closest images of the TNOs, which were returned unbinned (i.e., 1 × 1), as described in Weaver et al. (2021). All returned LORRI images are (or will be) available in FITS format (Pence et al. 2010) on the NASA Planetary Data System Small Bodies Node.

Most New Horizons LORRI images of distant TNOs were 4 × 4 binned images with exposure times of at least 10–64 s.

Table 1
List of the LORRI Observations of the 15 TNOs We Investigated in This Work

	Obs. Date	Dist. (au)	Phase
2004 LW_{31}	2019-09-03	1.068	106.626
2011 HF_{103}	2018-10-26	0.583	43.567
	2018-11-27	0.391	65.703
	2019-01-07	0.344	118.068
2011 HJ_{103}	2017-09-20	0.672	26.835
2011 HK_{103}	2018-08-17	0.290	50.679
	2018-09-10	0.253	95.916
	2018-09-28	0.332	123.956
2011 HZ_{102}	2018-11-07	0.335	21.002
	2018-11-22	0.228	34.591
	2018-11-27	0.202	41.031
	2018-11-30	0.185	47.156
2011 JA_{32}	2018-08-21	0.557	48.273
	2018-09-27	0.453	81.395
2011 JW_{31}	2018-08-19	0.354	16.631
2011 JX_{31}	2019-12-07	1.662	23.847
	2020-04-25	0.648	48.813
	2020-06-06	0.443	77.046
	2020-07-19	0.441	121.753
2011 JY_{31}	2018-08-20	0.277	27.197
	2018-09-10	0.149	61.816
	2018-09-17	0.135	85.063
	2018-09-30	0.170	122.361
2012 HE_{85}	2017-09-23	0.792	19.737
	2017-11-03	0.503	34.083
	2017-12-06	0.342	63.905
2012 HZ_{84}	2017-09-18	0.938	28.768
	2017-11-02	0.637	46.330
	2017-12-06	0.500	73.056
2014 OS_{393}	2019-01-06	0.092	85.078
	2019-01-09	0.098	100.475
2014 PN_{70}	2019-01-05	0.619	19.467
	2019-03-04	0.166	49.159
	2019-03-09	0.137	60.557
	2019-03-14	0.117	76.623
	2019-03-19	0.109	99.978
2018 MF_{13}	2019-09-02	2.177	80.961
2018 MG_{13}	2019-12-06	1.156	66.161

Note. Columns are observation date, TNO–spacecraft distance at observation (au), and Sun–TNO–spacecraft phase angle (degrees).

Prior to 2019, the LORRI flight software was only capable of accepting exposure times of up to 30 s. An updated version of the LORRI flight software was uploaded in spring 2019, after the completion of the Arrokoth flyby, which enabled substantially longer exposures of up to 64 s. Table 1 gives the observational circumstances for the 15 TNOs covered in this paper. Most were observed at multiple Sun–target–observer solar phase angles, which significantly helps to constrain their orbits. The New Horizons spacecraft spends most of its time in a passively spin-stabilized mode and must use propellant to despin in order to observe TNOs. The LORRI observations were therefore concentrated into a few designated "three-axis" periods. This allowed for wide coverage of the TNO's solar phase angles, but the spacecraft was not able to observe them all at the same phase angles. The 4×4 LORRI observations were generally of two types, either "light curve" or "phase." The light-curve observations typically consisted of 18 separate image sequences, spaced out by 1 hr, with two to five images per sequence, depending on the expected S/N of the target. Since the majority of known TNO light curves are shorter than 18 hr (Dotto et al. 2008; Benecchi & Sheppard 2013), these observations were intended to provide both the rotational period of the target TNO and the solar phase observation that could be corrected for rotational phase. The phase observations were typically taken when the S/N of the target was too low to perform a light-curve observation and typically consisted of four image sequences, 1 hr apart, of 20–50 images each. The phase observations were generally performed right after a target became brighter than $V = 20$ as the spacecraft was moving toward it or after the spacecraft had passed by the object and was viewing it at greater than 90° solar phase. The high phase observations were particularly challenging, as solar scattered light reduced the effective sensitivity of LORRI and introduced artifacts that needed to be subtracted from the images to allow for accurate astrometry and photometry.

The basic processing of the LORRI 4×4 images is similar to Porter et al. (2016) and Verbiscer et al. (2019) but improved over the years as we obtained and processed more data. First, we corrected the pointing of each image to correspond to the Gaia DR2 (Gaia Collaboration et al. 2018) stars in the field. Since the roll information in the header from telemetry is usually very good, and there is no atmospheric distortion to change the Simple Imaging Polynomial parameters, we initially fit an R.A./decl. offset for each image and then refined that with an R.A./decl./roll offset solution. For each individual image, we used the AstroPy (Astropy Collaboration et al. 2013) implementation of DAOPhot (Stetson 1987) to detect the point sources in the field that have roughly the FWHM that we expect for the LORRI PSF (≈5–8 original pixels, ≈1.1–1.5 4×4 binned pixels). We then matched up star patterns to the detected sources to produce an initial solution, typically good to better than half a pixel, depending on the number of stars. Because the New Horizons spacecraft is moving roughly radially from the Sun in the direction of Sagittarius, the star density of most observations is quite high, and there can be more than 300 Gaia DR2 stars brighter than $V = 20$ in the LORRI field of view. We next selected the brightest stars in the field (up to 30, regardless of whether they matched a source in the initial solution) and extracted an 11×11 pixel window centered on their predicted position with the initial solution. Next, we median-stacked those 30 star windows to produce an empirical measure of the shape of the PSF for the image and fit it with a 2D Gaussian distribution. While a 2D Gaussian is not a perfect model for the PSF, it allows us to capture the frequent cases where a pointing thruster burn mid-observation caused the effective PSF of the image to be smeared into a line. We next used the model PSF and fit an MCMC PDF for each star's position and brightness using the *emcee* package (Foreman-Mackey et al. 2013). We used the centers of the stars' PDFs to make an initial best fit, check for outliers and reject them, and then create a PDF for the R.A., decl., and roll solution. Finally, we saved a new version of the image with the mean of the PDF applied to the CRVAL1 (R.A.), CRVAL2 (decl.), and CDx _x (roll) parameters. The standard

deviation of the R.A./decl./roll cloud was also saved as a measure of the effective pointing uncertainty in that image. For all images used in this work, the 1σ pointing uncertainty was less than $0\farcs2$ and typically around $0\farcs1$. This is about as good as could possibly be expected from $\approx 4''$ pixels and shows the power of using Gaia DR2 stars as control points.

The second major step in analyzing LORRI 4×4 images was to produce windowed images that are a stack of subframes centered on the nominal position of the TNO from the ephemeris. These are similar to the shift stacks used for Earth-based data but with the added factor that the parallax from the relative motion of the spacecraft can be quite high, up to around one LORRI field of view per hour. Typically, these windows are 51×51 pixels and scaled up by a factor of 4 to match the original pixel scale. While the process above means that we know the pointing of the spacecraft to high precision, the uncertainty of both the orbit of the TNO and the location of the spacecraft may mean that its position within the LORRI images is not always known to high precision. We therefore used the uncertainty of the orbit cloud (see below) to determine the shape and size of the window. We aligned the roll of the window so that the uncertainty in the orbit was horizontal, so that high-uncertainty objects might have a window shape of a few hundred pixels wide by 51 pixels tall, while the low-uncertainty objects (after the orbit includes the LORRI astrometry) were simply 51×51 pixels. The first step of this was simply to extract a window for each image of the data set. Next, we used a similar procedure as described above to produce an empirical PSF for each image using up to 30 stars in the image. We then created a synthetic star background image for each window. This required taking every other image in the data set, reprojecting the images to the same WCS as the target, and stacking all the windows to produce an empirical model of the background as seen by LORRI. Since the stacks typically have a rounder PSF (averaging over thruster firings) than the individual images, we then use the optimal image subtraction process described above (Alard & Lupton 1998). We then created stacks of both of each individual image sequence (a few minutes long) and of the full observation (up to a day long), along with empirical PSFs for each image stack.

The third step in analyzing the LORRI 4×4 images was to produce an R.A./decl./magnitude PDF for each image sequence. We started with the stack of all the star-subtracted images in the full observation. Because the sky motion of the TNO is dominated by the motion of the New Horizons spacecraft, the shift rate of the images is mostly independent of the TNO's precise orbit. A TNO that is not precisely at the predicted location will have almost the same offset in pixel location in all of the images. We therefore used the stack of all images to fit the pixel location of the TNO and then projected that x/y cloud to the individual images. This was particularly useful for the light curve–style observation sequences, where the TNO may have only had an S/N of ≈ 2 in the individual image sequences but S/N ≈ 8 in the full stack. We found a best-fit x/y/flux solution for the full stack using a χ^2 function that shifted the empirical star PSF around to fit the stack. We then used *emcee* again to produce an x/y/flux cloud for the full stack. For each individual image sequence, we converted the full-stack x/y cloud to R.A./decl. using an image sequence stack WCS and then found the initial R.A./decl. mean and covariance matrix. We convolved this with the rms pointing uncertainty from the WCS solutions and an estimate of the 1σ New Horizons spacecraft uncertainty of 200 km to produce the final astrometric uncertainty. The spacecraft uncertainty was unimportant for most cases but did matter for some of the observations closer than 0.1 au from the TNO (200 km at 0.1 au is $\approx 2''$, or half a 4×4 pixel). We then took a subset of the x/y cloud, shifted the image sequence stack PSF to all of those locations, and found the best-fit flux for that offset. This forced photometry allowed us to measure the brightness and brightness uncertainty of the TNO, even in cases were it might have had an S/N too low to fit a full x/y/flux cloud. We then convolved these fluxes with the CCD noise, using the gain of 22 and read noise of 1.11 e^-/DN, divided by the square root of the number of images. Finally, we converted the fluxes to instrument magnitudes and added a zero-point of 18.94 to produce our magnitude and uncertainties. The final R.A./decl./magnitude solutions were saved in the same format as the Earth-based data and used for the orbit solutions presented below.

3. Heliocentric Orbit Determination

To fit the orbits, we used the same orbital fitting and uncertainty process as was successfully used to estimate the orbit of Arrokoth prior to its flyby in 2018–19 (Porter et al. 2018; Buie et al. 2020). We used the astrometric PDFs described above to create a function that estimated the log probability of a given orbit state vector and then used that to populate an orbital PDF with *emcee* (Foreman-Mackey et al. 2013). The orbits were parameterized as Cartesian state vectors (3D position and velocity) relative to the solar system barycenter in the ICRF (Ma et al. 1998, 2009) at a fixed epoch. We used the ICRF as the integration frame, as all of our astrometry was measured relative to Gaia star positions, which are defined relative to the ICRF (Gaia Collaboration et al. 2018). The epoch for most cases was at the time of the first observation, enabling the numerical integrator to only operate in a single direction (though the software is capable of allowing for an arbitrary epoch time). As our time base, we used JPL Ephemeris Time (ET), the linear seconds elapsed in Barycentric Dynamical Time (TDB) starting at 2000 January 01 00:00:00 TDB. This is both the standard used by JPL SPICE and convenient for converting dynamical simulations to observations. Defining the state vector relative to the solar system barycenter is the most logical option from a dynamical point of view, as we did not model any extrasolar perturbations, but it does require choosing a defined solar system barycenter and initial conditions for the solar system. We used the JPL NAIF DE430 solar system solution (Folkner et al. 2014) for all orbit solutions presented here, reading it with the *spiceypy* library (Annex et al. 2020b). To predict the expected astrometry at each observation time, we first created a solar system object that has the Sun and eight perturbing planets that are defined in DE430, as well as the TNO, which is assumed to be massless. We used a high-order Runge–Kutta–Nyström orbit integrator based on Brankin et al. (1989), converted to C++[9]; this is the same as described in Porter et al. (2016, 2018). We first integrate the solar system (including the TNO) to the observation times and then use those positions to estimate the observer–TNO distances, and thus light-time corrections, for each observation. We then rerun the integration to the observation times minus the estimated light-time and use those

[9] https://github.com/ascendingnode/PyNBody

positions to estimate the R.A./decl. of the TNO as seen by the observer. While not a fully converged light-time correction, this is sufficient for slow-moving TNOs. With these predicted astrometric positions for all of the observations, we can then estimate the log probability of each predicted position. We estimate this for each observation as

$$\text{logprob}_i = -\frac{1}{2}((O_i - E_i)(K_i^{-1})(O_i - E_i)^T) + ln(|K_i|) + 2\,ln(2\pi), \quad (1)$$

where $O_i - E_i$ is the difference between the mean observed position and the predicted position, and K_i is the R.A./decl. covariance matrix for the observation. The rightmost two terms were precomputed and stored, while the first term was computed for each probability estimation. The total probability function takes a given state vector, assesses whether it meets any priors imposed on the orbit (e.g., inclination less than 90°), and, if so, computes the predicted astrometric positions for each observation time. It then uses these to find the log probability for each observation and finally returns the sum of the log probabilities. If the state vector fails any test (i.e., violates a prior), a log probability of $-\inf$ is returned to communicate that the solution is invalid. This log probability function is sufficient to run an MCMC estimation of the orbital uncertainty using *emcee*. In addition, because the log probability is proportional to the negative of the χ^2, we can define a simple function that returns the negative of the log probability and use that with the *scipy* (Virtanen et al. 2020) implementation of the downhill simplex function minimization (Nelder & Mead 1965) to find an initial best-fit state vector for each object. We then take the best-fit state vector and perturb it slightly to produce 100 "walkers" that will be used as initial conditions for the MCMC estimation. Initially, we run *emcee* for 3000 iterations and then check for convergence. If the cloud is not converged, then 100 states from the old cloud are taken as walkers for a new cloud, and the new cloud is rerun for three times the number of iterations as the old. This process is repeated until *emcee* reports that convergence is reached. We found that 3000 iterations was sufficient for nearly all of the objects in this work, and 9000 iterations was sufficient for the remainder. This full discrete PDF of the state vectors at the epoch is then saved as a *numpy* object. Finally, to make the cloud more widely usable, we created a NAIF SPICE SPK Type 3 kernel. Type 3 SPK kernels define the position and velocity of an object relative to another object and are stored as Chebyshev polynomials (Tchebychev 1853). We take the full PDF cloud of states and evolve them using the high-precision integrator for 10 yr before the first astrometric observation and 10 yr after the last astrometric observation, with a time interval sufficient to capture the motion of the object. We then take the average state vector at each of those times and use it calculate 27th-order Chebyshev polynomials, which can then be passed to a custom CSPICE wrapper to write the SPICE kernel. In our testing, our SPICE kernels are typically accurate to within 1 km of the mean of the full solution, much less than the uncertainty for any of the objects.

The full state vectors and 1σ uncertainty for all 15 objects can be seen in Table 4 in the Appendix. The inclusion of LORRI data in the solutions placed strong constraints on the locations of the objects at the time of the observation by New Horizons; see Table 1. The relative effect that this had on each object depended on the quality of the Earth-based data, but generally, the uncertainty in the positions of the TNOs at the time of the LORRI observations was smaller than a few thousand kilometers relative to the solar system barycenter, with uncertainties increasing with time since then.

We categorized the 15 TNOs with the criteria from Bannister et al. (2018) by integrating the mean orbit for each object backward in time for a million years, and we present the mean elements in Table 3. Most of the objects fall into the "Main Belt" category of Bannister et al. (2018), meaning that they are likely to be components of the classical Kuiper Belt. Object 2018 MG_{13} appears to be at the 2:1 9:5 mean-motion resonance with Neptune. Likewise, 2012 HE_{85} appears to be at the 9:5 mean-motion resonance with Neptune. However, they both have low eccentricities and inclinations and are located in the middle of the main Kuiper Belt, so they are possibly classical KBOs that were later trapped into resonances. Object 2011 HK_{103} is the one of the 15 that is arguably separate from the main Kuiper Belt. It has a semimajor axis of 53.2 and eccentricity of 0.31, making it a member of the "detached-component" population. Object 2011 HK_{103} is thus much more representative of the bodies that New Horizons can observe in the future, while the remaining objects provide context to understand the main-belt object Arrokoth.

4. Occultation Predictions

4.1. Occultation Prediction Process

To predict the occultation opportunities presented here, we used the orbit state vector cloud described above, as well as the mean position SPICE kernel, in conjunction with Gaia EDR3 star positions. For each object in Table 3, we used a combination of ground-based, HST, and New Horizons photometry to calculate an approximate absolute magnitude H_V. We then combined this with an approximation of the albedo of the object as 5% (broadly consistent with most scattered TNOs; Santos-Sanz et al. 2012) to estimate the approximate diameter of the projected shape of the object. While this should not be treated as a precise estimate of the size of the TNOs, it is sufficient to enable planning of the occultation observations that would be able to measure the actual projected sizes of the TNOs. While the astrometric analysis of the images described above was performed entirely with Gaia DR2, by the time we were searching for occultation opportunities, Gaia EDR3 was available (Lindegren et al. 2020). The EDR3 is very similar to DR2 but has slightly refined star positions, which make it the best to use for this analysis. To search for potential occultation opportunities over a given time period, we started by breaking the search interval into days and finding the R.A. and decl. of the TNO as seen from the center of Earth at 100 points between the start and end of that 24 hr period. We also use the mean distance between the Earth and TNO in the 24 hr period to calculate the angular radius of a circle with a physical radius of 10^5 km. We can then construct an ADQL query to find the Gaia EDR3 stars contained within the calculated angular radius from the 100 points, in order to fully capture any stars that the TNO may pass close to. We also add the conditions that the EDR3 stars must have: (1) values for proper motion that are not NULL, (2) more than 80 good observations, and (3) less than five bad observations. These conditions allow us to filter out any poorly

defined sources from the ERD3 catalog. We send this ADQL query to the Gaia TAP+ server using the *astroquery.gaia* library (Ginsburg et al. 2019) and then save the result in a structured *numpy* file. After performing this search and saving stars for the entire time period, we then load all of the cached star files, concatenate them, and remove duplicates. We can then iterate through all of the stars to determine which ones are potential occultation targets. We do this by finding the time over the search period on which the star is closest to the TNO as seen from the center of the Earth. To do this, we not only use the SPICE kernel to find the apparent R.A./decl. of the TNO at a given time, but we also use the Gaia proper motion and parallax to correct the star's position at that time. We then find the angular distance from the TNO to the star as seen from the geocenter at that time and use the TNO–Earth distance to convert that to a physical distance corresponding to the minimum cross-track offset of the center of the Earth. If this distance is less than the radius of the Earth, then an occultation observation is possible. We save all of the results, along with the star magnitude, to an *SQLite* database. Once all stars have been searched for their minimum distance as described, we then calculate detailed occultation tracks for just the stars that have small enough geocenter cross tracks and were brighter than the given magnitude cutoff. Starting with the nominal time of minimum distance found above and the relative speed of the TNO compared to Earth in the plane of the occultation, we estimate a rough time for the TNO's shadow to cross the Earth. For every whole second of this time period, we attempt to calculate the location of the TNO's shadow on the Earth. We start by finding the state vector from the center of Earth to the TNO at that time. We then use this to define the occultation frame, such that the $\hat{k}$-axis is aligned with the Earth–TNO vector, and the $\hat{j}$-axis is aligned with the TNO–Earth relative velocity vector. In this frame, the $\hat{i}$-axis defines the cross-track offset, and the $\hat{j}$-axis defines the down-track axis. With these three orthonormal bases, we can define a rotation matrix from the occultation frame to the ICRF. We then find the star position at the point in time, applying all appropriate proper-motion and parallax corrections. We convert the star's astrometric location to an ICRF unit vector and then to a unit vector in the occultation frame using the rotation matrix. We then find the distance from the TNO to the $\hat{i} \times \hat{j}$ occultation plane along the star direction vector. This can then be used to find where the star is in the occultation frame and thus what the instantaneous cross- and down-track distances are at that time. If the magnitude of the cross-/down-track vector is larger than the size of the Earth, then the center of the TNO's shadow is not on the Earth, and the point is abandoned. If, however, the cross-/down-track vector is small enough, we then find its location on the surface of the Earth. We convert the cross-/down-track vector from the occultation frame to the ICRF and then from the ICRF to the rotating frame of Earth. If possible, we use the current JPL NAIF SPICE kernel for the rotation of the Earth in the International Terrestrial Rotation Frame (Altamimi et al. 2016), the highest-precision Earth rotation kernel available. However, if the occultation time is beyond the coverage of that kernel, we use the "Iau_Earth" frame in SPICE. We do the same for the star vector and then find where the star vector emanating from the cross-track point intersects the surface of the Earth using the WGS84 geoid for the shape of the Earth. This, finally, is the location on the Earth's surface of the center of the TNO's shadow. Repeating this process allows us to build up a second-by-second track of the TNO's shadow's path across the surface of the Earth. To find the uncertainty in this path, we go to the time when the down track is zero for the mean orbit and repeat the process for the large-orbit PDF cloud, finding the cross-/down-track vector of the TNO for the cloud in the frame of the mean orbit's occultation. The standard deviation of the cross tracks of the cloud tells us the 1σ uncertainty in the cross track of the occultation in kilometers. Likewise, taking the standard deviation of the down-track distances divided by the occultation velocity provides the 1σ uncertainty in the timing of the occultation. Finally, we can plot our results to produce Table 2 and Figures 1–4. We used the *cartopy* package to plot the Earth as seen from the TNO in an orthographic projection. To plot the nominal path of the object, we used the procedure described above but either adding or subtracting the nominal radius of the object from the cross track before finding each ground track. This is plotted as the red region in the occultation figures. We then plotted the radius $\pm 1\sigma$ uncertainty area with the same process; these are plotted as the yellow regions in the occultation figures.

4.2. Practicality of Occultation Observability

While we found a large number of observable occultations, most are likely not practical to observe for a variety of reasons. The most basic technical restriction is on the brightness of the star. The brighter the star, the shorter the integration time to take an image with a sufficient S/N that an occultation can be detected. In practice, this means that occultations of TNOs with velocities of $\approx$10–20 km s^{-1} are just barely possible with 16 inch aperture telescopes, as shown by the Arrokoth occultations in 2017–2018 (Buie et al. 2020). Thus, for our TNOs, most occultations of stars dimmer than $V = 16$ are not practical with modern portable telescopes with 16 inch or smaller aperture sizes. Next, the occultation path must cross over land at night. While daytime occultation observations of very bright stars (i.e., Sirius) may occasionally be possible for main-belt asteroids, TNO occultations of very bright stars are far too infrequent for this to be practical. Lunar scattered light, and therefore lunar elongation, is another concern, as it raises the background level of the sky and reduces the depth of stars that can be observed. Further, to the best of our knowledge, no successful TNO occultation has been captured from an oceangoing vessel, though single-chord occultations have been observed of Pluto and Arrokoth by the NASA/DLR SOFIA flying observatory while over open water (Buie et al. 2020; Person et al. 2021). A further geographic consideration is the typical climatic conditions of an occultation site, as there is little point to sending a telescope to an area that is almost guaranteed to be cloudy. One evaluation of this is to look at a potential occultation site in satellite or aerial imagery; if it is green and verdant, it is likely to be cloudy at night. Finally, there are political and public health considerations. Many occultations occur in areas where it is either not practical or not advisable for US or European occultation teams (who have performed most occultation observations to date) to travel. We hope that some of these and other occultation opportunities may in the future be observed by groups from outside the US and Europe, including the members of the International Occultation Timing Association (IOTA[10]). Before 2020, public health considerations against travel tended to be localized, and we expect that as COVID-19 recedes, this will eventually become the case again. Regardless, however, occultation travelers must comply with public health directives, which

[10] https://occultations.org

Table 2
The 66 Occultation Opportunities for the 15 TNOs Analyzed in This Work

	Date (UTC)	R.A.	Decl.	Mag.	Mean Lat.	Mean Lon.	Uncert.
2004 LW_{31}	2022 Jul 12 18:57:56	$19^h29^m18\overset{s}{.}01192$	$-21°03'49\overset{''}{.}10313$	13.9	46°50′S	81°08′E	1427
	2022 Jun 20 05:16:32	$19^h31^m01\overset{s}{.}94081$	$-20°59'55\overset{''}{.}33476$	15.5	34°39′N	63°00′W	1397
	2022 Sep 09 16:57:42	$19^h25^m30\overset{s}{.}32245$	$-21°12'52\overset{''}{.}10789$	13.4	38°37′S	51°07′E	1570
	2024 Jul 18 20:43:08	$19^h39^m28\overset{s}{.}49815$	$-20°48'39\overset{''}{.}79541$	15.7	28°40′S	48°00′E	1764
	2026 Jul 04 13:30:32	$19^h51^m19\overset{s}{.}74722$	$-20°26'34\overset{''}{.}72000$	15.9	38°45′N	66°06′E	2112
	2027 Nov 24 16:36:04	$19^h52^m58\overset{s}{.}20040$	$-20°28'40\overset{''}{.}11748$	13.9	29°41′S	12°56′W	2181
2011 HF_{103}	2024 Aug 19 11:47:16	$19^h34^m33\overset{s}{.}44436$	$-19°39'22\overset{''}{.}05258$	15.2	23°38′N	95°14′E	366
	2024 Dec 11 22:37:23	$19^h36^m29\overset{s}{.}47991$	$-19°40'23\overset{''}{.}42017$	13.8	28°04′N	111°58′W	405
	2024 May 16 09:47:44	$19^h41^m06\overset{s}{.}03435$	$-19°23'55\overset{''}{.}27145$	15.6	14°28′S	86°36′W	409
	2024 Oct 27 16:06:35	$19^h33^m23\overset{s}{.}15647$	$-19°45'29\overset{''}{.}01801$	15.8	33°51′N	12°34′E	442
	2025 Feb 24 12:48:19	$19^h44^m05\overset{s}{.}76542$	$-19°22'24\overset{''}{.}00161$	14.7	45°16′N	63°42′W	390
	2026 Aug 13 08:28:46	$19^h45^m42\overset{s}{.}81406$	$-19°18'37\overset{''}{.}88212$	15.0	7°28′N	52°37′W	454
	2026 Jul 03 17:41:56	$19^h48^m52\overset{s}{.}96406$	$-19°09'53\overset{''}{.}11965$	15.2	46°00′N	97°15′E	472
	2027 Nov 06 12:01:59	$19^h49^m23\overset{s}{.}18022$	$-19°16'16\overset{''}{.}13595$	13.9	5°26′N	69°23′E	621
2011 HJ_{103}	2022 Jun 07 09:27:30	$19^h42^m41\overset{s}{.}62766$	$-20°04'23\overset{''}{.}63470$	16.0	4°14′N	102°55′W	1354
	2023 Oct 25 02:08:58	$19^h42^m01\overset{s}{.}02903$	$-20°19'32\overset{''}{.}63708$	13.7	10°54′N	102°38′W	1167
2011 HK_{103}	2022 Jun 04 10:56:15	$19^h35^m54\overset{s}{.}24881$	$-20°29'56\overset{''}{.}22751$	15.5	42°24′S	70°59′W	200
	2022 Jun 15 07:51:36	$19^h35^m11\overset{s}{.}02555$	$-20°31'43\overset{''}{.}07593$	15.7	37°40′N	97°29′W	201
	2022 Jun 15 20:19:06	$19^h35^m08\overset{s}{.}79882$	$-20°31'48\overset{''}{.}60398$	14.0	51°15′S	89°07′E	203
	2023 Aug 17 13:47:37	$19^h36^m36\overset{s}{.}54908$	$-20°40'16\overset{''}{.}84821$	15.2	4°01′N	104°37′E	278
	2024 Aug 08 07:14:38	$19^h43^m41\overset{s}{.}53518$	$-20°33'12\overset{''}{.}38209$	12.2	46°34′S	64°19′W	330
	2024 Jul 10 04:27:07	$19^h46^m05\overset{s}{.}40448$	$-20°26'17\overset{''}{.}51683$	14.5	12°47′N	64°25′W	321
	2028 Jul 17 16:27:54	$20^h12^m01\overset{s}{.}26961$	$-19°55'43\overset{''}{.}69050$	15.3	33°46′N	107°43′E	598
2011 HZ_{102}	2023 Oct 27 11:36:03	$19^h30^m29\overset{s}{.}38732$	$-20°11'24\overset{''}{.}90863$	14.5	46°34′N	78°16′E	94
	2025 Aug 16 23:01:39	$19^h42^m43\overset{s}{.}15764$	$-19°44'57\overset{''}{.}22835$	15.6	45°11′N	29°16′W	437
	2026 Nov 19 16:49:08	$19^h47^m35\overset{s}{.}54908$	$-19°38'47\overset{''}{.}26578$	13.6	15°27′S	14°30′W	219
2011 JA_{32}	2025 Aug 14 03:49:42	$19^h46^m12\overset{s}{.}68243$	$-18°18'21\overset{''}{.}46489$	14.4	5°24′S	86°02′W	2271
	2027 Sep 03 00:27:20	$19^h56^m37\overset{s}{.}70321$	$-17°46'03\overset{''}{.}71905$	13.8	20°30′N	57°54′W	2327
2011 JW_{31}	2025 Jul 30 06:41:29	$19^h47^m03\overset{s}{.}30800$	$-19°13'03\overset{''}{.}89548$	11.6	40°55′S	79°09′W	1488
	2027 Aug 14 01:27:42	$19^h57^m34\overset{s}{.}75240$	$-18°44'31\overset{''}{.}90890$	15.9	49°03′S	37°59′W	1844
	2027 Oct 17 12:27:56	$19^h55^m13\overset{s}{.}28601$	$-18°53'31\overset{''}{.}61940$	13.2	44°22′S	84°29′E	1486
2011 JX_{31}	2023 May 20 16:00:59	$19^h26^m57\overset{s}{.}89952$	$-20°15'11\overset{''}{.}82855$	13.9	0°17′N	17°15′E	161
	2023 Nov 15 17:57:39	$19^h21^m01\overset{s}{.}44781$	$-20°31'14\overset{''}{.}32536$	15.7	22°51′S	33°27′W	178
	2024 Jun 06 20:59:37	$19^h30^m33\overset{s}{.}67817$	$-20°10'30\overset{''}{.}05527$	16.0	8°23′S	80°34′E	206
	2029 Jul 04 08:59:09	$19^h51^m03\overset{s}{.}22613$	$-19°37'29\overset{''}{.}79560$	15.7	26°09′N	112°20′W	465
	2029 Mar 15 09:34:04	$19^h52^m45\overset{s}{.}66343$	$-19°34'25\overset{''}{.}73376$	15.6	40°14′S	14°48′W	510
2011 JY_{31}	2021 Nov 15 06:16:11	$19^h21^m45\overset{s}{.}46409$	$-19°53'13\overset{''}{.}96286$	13.6	5°46′N	86°32′E	218
	2022 Jun 08 02:54:23	$19^h32^m50\overset{s}{.}13617$	$-19°24'18\overset{''}{.}66454$	15.2	27°34′S	6°04′W	262
	2022 Mar 12 09:10:48	$19^h33^m06\overset{s}{.}98629$	$-19°28'27\overset{''}{.}25508$	14.5	3°47′S	17°25′W	129
	2023 Sep 15 22:37:55	$19^h31^m39\overset{s}{.}83285$	$-19°25'42\overset{''}{.}19779$	15.6	19°49′S	41°31′W	153
	2026 May 29 15:28:55	$19^h55^m59\overset{s}{.}77855$	$-18°19'24\overset{''}{.}41768$	15.9	35°17′S	7°28′W	653
	2026 Nov 27 09:49:04	$19^h50^m07\overset{s}{.}66255$	$-18°39'01\overset{''}{.}89490$	12.7	38°17′N	75°50′E	490
	2027 Aug 17 20:05:27	$19^h55^m48\overset{s}{.}62976$	$-18°17'09\overset{''}{.}16582$	12.9	15°49′N	25°15′E	289
2012 HE_{85}	2021 Nov 13 01:21:43	$19^h26^m46\overset{s}{.}73053$	$-19°25'26\overset{''}{.}19861$	16.0	21°31′N	88°38′W	705
	2022 Aug 19 12:32:44	$19^h33^m06\overset{s}{.}96639$	$-19°04'31\overset{''}{.}82501$	15.6	45°26′S	48°27′E	736
	2022 Dec 09 04:43:35	$19^h35^m01\overset{s}{.}69949$	$-19°05'42\overset{''}{.}21887$	15.8	12°00′N	87°36′E	825
	2023 Sep 03 15:59:40	$19^h38^m26\overset{s}{.}79402$	$-18°50'07\overset{''}{.}42599$	14.9	26°23′S	73°19′E	818
	2024 Dec 08 16:39:07	$19^h46^m55\overset{s}{.}66480$	$-18°31'45\overset{''}{.}94955$	15.7	18°13′S	31°01′W	1110
	2025 Jul 16 23:30:20	$19^h54^m20\overset{s}{.}66839$	$-18°03'21\overset{''}{.}43763$	13.1	14°22′N	6°00′E	1178
	2025 Jun 14 07:13:38	$19^h56^m53\overset{s}{.}89475$	$-17°57'09\overset{''}{.}18336$	15.9	11°22′N	75°33′W	1267
	2028 Aug 04 23:42:40	$20^h11^m00\overset{s}{.}43241$	$-17°07'35\overset{''}{.}47303$	15.7	32°06′S	4°02′W	1523
	2029 Jul 05 10:31:47	$20^h19^m33\overset{s}{.}02254$	$-16°38'10\overset{''}{.}06712$	13.2	53°23′S	61°27′W	1816
2012 HZ_{84}	2025 Feb 22 03:51:27	$19^h55^m43\overset{s}{.}05265$	$-17°18'20\overset{''}{.}02831$	12.6	23°38′S	89°50′E	2476
	2027 Jul 13 22:29:40	$20^h08^m12\overset{s}{.}91088$	$-16°14'33\overset{''}{.}98768$	14.4	12°36′N	28°41′E	4415
	2027 Jun 15 22:59:56	$20^h10^m22\overset{s}{.}64104$	$-16°09'27\overset{''}{.}19483$	14.1	15°52′S	53°46′E	5295
	2027 Mar 19 09:52:19	$20^h10^m18\overset{s}{.}00446$	$-16°19'19\overset{''}{.}72660$	15.7	35°25′S	17°08′W	2432
2014 OS_{393}	2023 Jun 06 07:23:28	$19^h36^m55\overset{s}{.}15527$	$-19°49'14\overset{''}{.}86495$	16.0	31°43′N	78°04′W	78

Table 2
(Continued)

	Date (UTC)	R.A.	Decl.	Mag.	Mean Lat.	Mean Lon.	Uncert.
2014 PN_{70}	2022 Aug 10 21:20:43	$19^h24^m33\overset{s}{.}07421$	$-20°09'37\overset{''}{.}31921$	14.9	16°27′N	6°01′E	80
	2023 Aug 13 07:08:11	$19^h29^m50\overset{s}{.}34844$	$-20°03'34\overset{''}{.}11058$	13.5	51°01′N	121°53′W	103
	2024 Jul 30 22:25:53	$19^h36^m12\overset{s}{.}05402$	$-19°54'00\overset{''}{.}44927$	14.6	11°24′S	7°11′E	126
	2025 May 20 09:49:48	$19^h46^m34\overset{s}{.}34010$	$-19°33'46\overset{''}{.}08400$	15.3	41°07′S	80°57′W	145
2018 MF_{13}	2023 Jun 19 19:47:51	$19^h37^m57\overset{s}{.}72177$	$-22°09'31\overset{''}{.}20942$	12.5	8°27′N	85°04′E	2893
	2027 May 28 06:55:13	$19^h59^m09\overset{s}{.}04301$	$-21°29'40\overset{''}{.}99688$	14.4	27°05′N	60°07′W	4783
2018 MG_{13}	2022 Sep 10 11:02:52	$19^h25^m33\overset{s}{.}61354$	$-20°26'11\overset{''}{.}07520$	13.8	52°02′N	111°45′E	1932
	2023 Nov 04 00:10:10	$19^h30^m49\overset{s}{.}55310$	$-20°30'38\overset{''}{.}59692$	15.7	35°19′S	87°57′W	1962
	2026 Nov 03 18:36:29	$19^h45^m38\overset{s}{.}77917$	$-20°32'27\overset{''}{.}07981$	15.9	4°41′S	26°45′W	3672

Note. Columns are occultation mid-time (UTC), R.A. (ICRF), decl. (ICRF), star magnitude (Gaia *G*), latitude of the middle of the occultation path, longitude of the middle of the occultation path, and 1σ cross-track uncertainty in kilometers.

Table 3
The 15 TNOs We Investigated in This Work with Mean Orbital Elements after Integrating for 10^6 yr

	Arc (yr)	H_V	*a* (au)	*e*	*I* (deg)	Classification
2004 LW_{31}	15.2	7.1 ± 1.1	46.4962	0.07938	2.5739	Main belt
2011 HF_{103}	9.3	7.8 ± 0.5	43.0024	0.05437	2.0293	Main belt
2011 HJ_{103}	6.4	8.3 ± 0.3	46.5437	0.15223	4.7306	Main belt
2011 HK_{103}	7.4	7.9 ± 0.5	53.1782	0.30776	6.1247	Detached component
2011 HZ_{102}	7.6	8.8 ± 0.5	43.1878	0.01188	1.4116	Main belt
2011 JA_{32}	7.4	9.1 ± 0.4	46.5912	0.13000	2.9657	Main belt
2011 JW_{31}	7.3	8.3 ± 0.4	45.5794	0.09231	1.3488	Main belt
2011 JX_{31}	9.2	7.6 ± 0.5	44.9503	0.11577	2.5036	Main belt
2011 JY_{31}	7.4	8.1 ± 0.2	43.9859	0.05331	2.3809	Main belt
2012 HE_{85}	5.6	9.1 ± 0.3	44.4961	0.09575	2.8715	Resonant 9:5
2012 HZ_{84}	6.6	9.4 ± 0.5	45.9529	0.18893	5.6124	Main belt
2014 OS_{393}	5.5	9.9 ± 0.7	44.0740	0.01742	2.9968	Main belt
2014 PN_{70}	7.2	10.1 ± 0.6	44.2189	0.05700	3.3276	Main belt
2018 MF_{13}	15.1	7.9 ± 0.8	41.1361	0.24067	2.9991	Main belt
2018 MG_{13}	2.5	7.5 ± 0.3	47.6716	0.03550	9.6975	Resonant 2:1

Note. Columns are observation arc length (yr), absolute magnitude and uncertainty, mean semimajor axis (au), mean eccentricity, mean ecliptic inclination (deg), and classification based on the OSSOS classification (Bannister et al. 2018). For the full state vectors, see Table 4.

makes international travel inadvisable in 2021 and likely into 2022 as well. With all of these considerations in mind, we present below the occultation opportunities we think are the most practical to observe in 2021–2029.

4.3. US Domestic Occultation Opportunities

In general, there are not many occultation opportunities in the United States for objects that have been observed by New Horizons. This is because the New Horizons spacecraft is traveling almost radially out from the Sun in a direction of roughly R.A. = 288°, decl. = −20°. Any TNO that passes close to the spacecraft is close to this point in the sky and therefore very low on the horizon as seen from North America. Nonetheless, there are a few occultations that may be visible from the United States. These are valuable in times of reduced international travel; see Figures 1 and 2.

The earliest two occultation opportunities that we have identified are of 2011 JY_{31} and 2012 HE_{85} in 2021 November; see Figure 1. The occultation of 2011 JY_{31} on 2021 November 15 UTC is particularly interesting, as the nominal centerline passes over the island of Hawaii, home to many large telescopes. Object 2011 JY_{31} has been identified as a potential close binary with a separation of roughly 200 km (Weaver et al. 2021), which makes a successful observation of this event event more challenging but potentially quite rewarding. Leiva et al. (2020) were able to detect that 2014 WC_{510} is a similarly close binary (roughly 350 km separation) with a stellar occultation, albeit with a much wider network than would be possible for this event. The other 2021 event of interest is the occultation of 2012 HE_{85} on 2021 November 13 UTC. This event nominally passes over Baja California, northern Mexico, and southern Texas. However, the uncertainty for this event is rather high, with a cross-track uncertainty of 705 km, and the star only has a brightness of $G = 15.966$, barely brighter than our limit of $G = 16$. This event is not practical to observe without additional astrometry of 2012 HE_{85}, preferably from HST, and even then would require portable telescopes with relatively large apertures (16 inches/40 cm or larger) to reach a sufficient S/N for detection.

There are two North American occultation events of interest in 2022 June, 5 days apart, of 2004 LW_{31} and 2011 HK_{103}; see Figure 1. The 2004 LW_{31} event on 2022 June 6 UTC has a nominal path that passes over the southern United States but with a very large cross-track uncertainty of 1400 km. The 2011 HK_{103} path is slightly further north, passing from southern

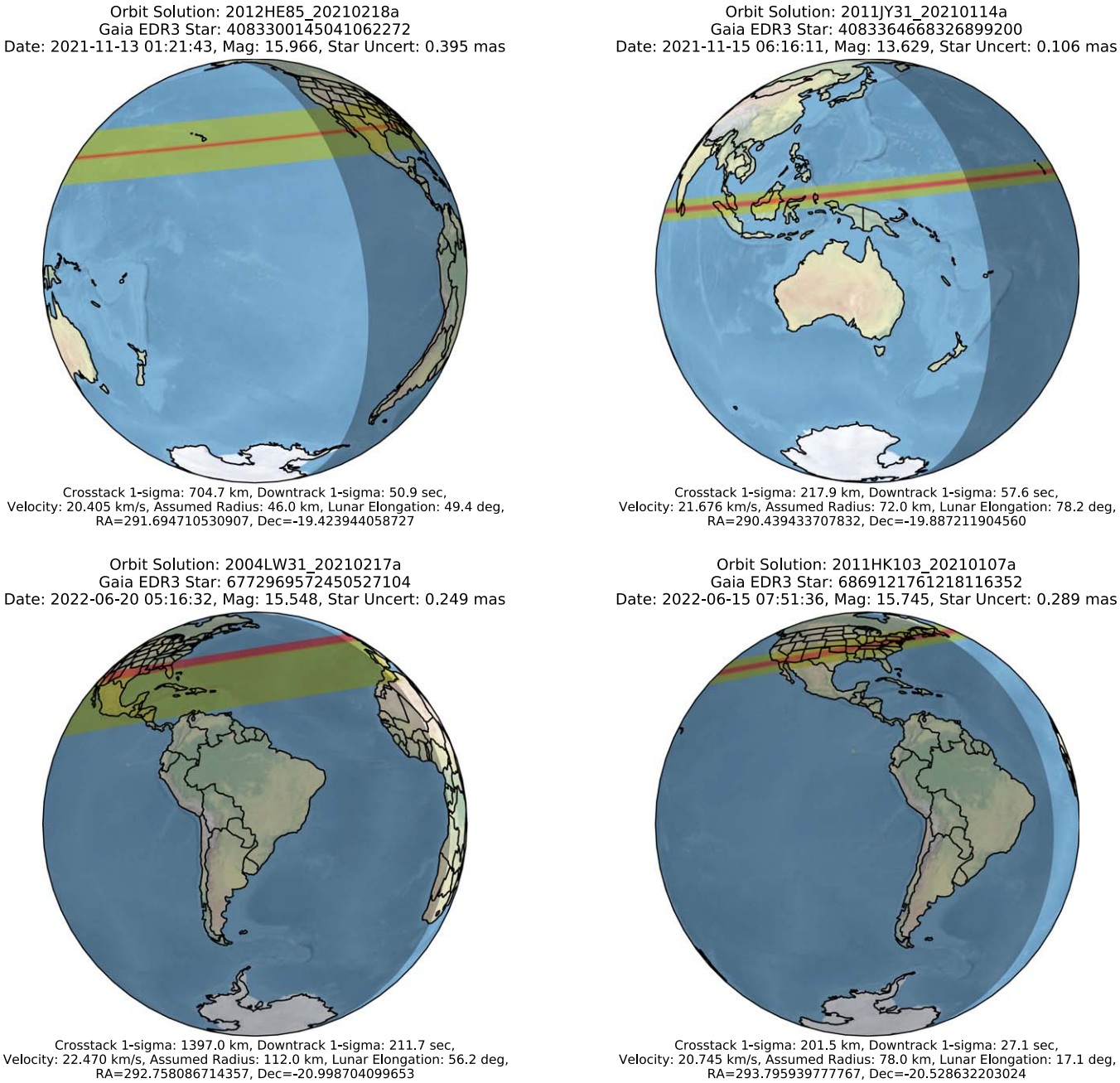

Figure 1. Best US domestic occultation opportunities for 2021–2022. The red region represents the nominal shadow path based on the size of the object, and the yellow region adds 1σ uncertainty. Note that the 1σ uncertainty for 2004 LW_{31} goes off of the disk of the Earth.

California to the northeastern United States and maritime Canada. The cross-track uncertainty for 2011 HK_{103} is considerably less, at 201 km. This is small enough to know that the track is observable but not enough to plan an occultation campaign. Both 2004 LW_{31} and 2011 HK_{103} would benefit from additional astrometry in late 2021/early 2022, especially from HST. If that astrometry is available and reduces the uncertainty in the tracks to less than 100 km, then the next major challenge to observe these events would be the star brightness ($G = 15.5$ and 15.7) and the proximity of the Moon, 56° and 17° away. Observation of these events thus requires deployment of large portable telescope systems. This might not be worth it for a single event; however, the nominal tracks for both events intersect in northern Texas. If those tracks are not significantly shifted after obtaining additional astrometry of 2004 LW_{31} and 2011 HK_{103}, then it would be possible to deploy a set of telescopes to Texas to observe both events. In addition, the 2011 HK_{103} event covers such a large stretch of the United States that amateur observers (e.g., IOTA) could provide a wide observation grid with robustness to variations in weather.

On 2023 June 6 UTC, there is an occultation of 2014 OS_{393} that passes over Baja California, northern Mexico, southern Texas, and central Florida; see Figure 2. Because we have a large amount of HST astrometry for 2014 OS_{393}, the 1σ cross-track uncertainty is only 78 km, roughly the size of the TNO. However, this would still be a very challenging event to observe, as the star is very faint ($G = 15.95$), and it is only 10°

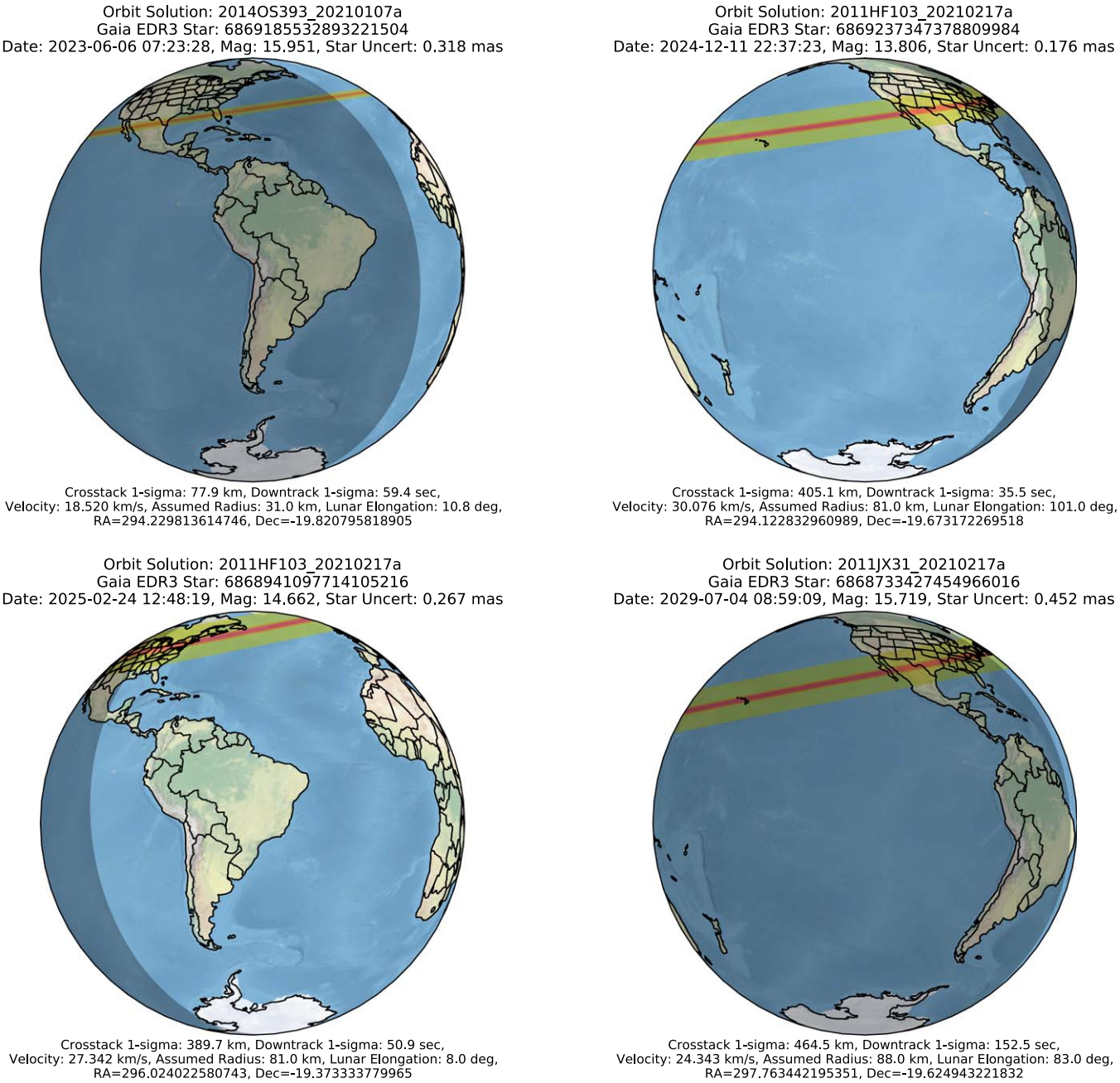

Figure 2. Best US domestic occultation opportunities for 2023–2029. The red region represents the nominal shadow path based on the size of the object, and the yellow region adds 1σ uncertainty.

away from the Moon at the time. Object 2014 OS_{393} is a very interesting target, though, as it was identified in New Horizons LORRI images as a potential very tight binary with a separation of roughly 200 km (Weaver et al. 2021). If the 2011 HK_{103} occultation in 2022, which has a similarly faint star close to the Moon, were successful, then that would pave the way for this event to be observed.

There are two occultations visible from the United States of 2011 HF_{103}, on 2024 December 11 and 2025 February 24 UTC; see Figure 2. The December event is visible shortly after sunset in the northeastern US, while the February event is visible shortly before sunrise in the midwestern US. They are both of relatively bright stars ($G = 13.8$ and 14.6), though the February event is only 8° from the Moon. These are both very challenging events and would not be worth pursuing if they were not occurring in areas with a large number of experienced occultation observers. The December event requires observation of a star that is very low in the sky right after it becomes visible, shortly after sunset. This is possible but requires a faster alignment of the telescope than may be practical in many cases. The February event is more practical in that the telescope has plenty of time to be aligned, but scattered light from the Moon will reduce sensitivity.

We were not able to identify any good US domestic occultation opportunities for 2026–2028. There will, however, be an occultation of 2011 JX_{31} on 2029 July 29 UTC visible from the US; see Figure 2. Its nominal path will pass over Hawaii, Baja California, northern Mexico, Texas, and the southeastern US. The 1σ cross-track uncertainty is 465 km, though this will reduce with any astrometry from 2021–2029,

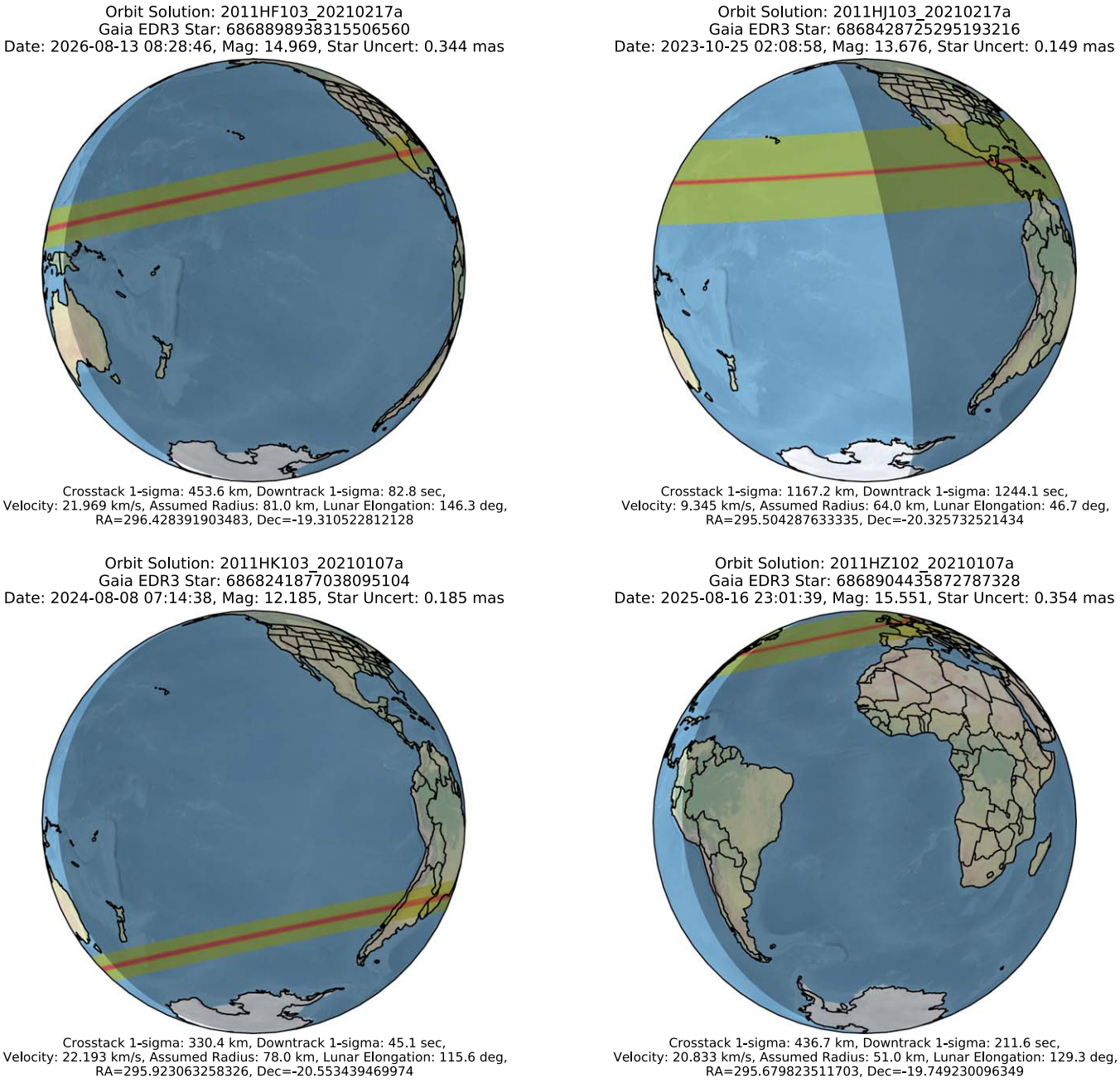

Figure 3. Best international occultation opportunities for 2011 HF_{103}, 2011 HJ_{103}, 2011 HK_{103}, and 2011 HZ_{102}. The red region represents the nominal shadow path based on the size of the object, and the yellow region adds 1σ uncertainty.

and the star brightness is $G = 15.7$. This is a very plausible event to observe from both Texas and Mexico and highly motivates future astrometric follow-up of 2011 HF_{103}.

4.4. International Occultation Opportunities

We were able to find five good non-US occultation opportunities for 2004 LW_{31}, as shown in Figure 4. Of these, the first two are in Australia in 2022; then there is an event that is possibly visible in South Africa in 2024, an event that passes over Japan in 2026, and an event in southeastern Africa and Madagascar in 2027. All of these events have large uncertainties and would require additional astrometry, preferably from HST, to become viable events to target.

We were able to find six good non-US occultation opportunities for 2011 HF_{103}, as shown in Figures 3 and 4. Three events are in 2024, visible in central South America, the Philippines and Vietnam, and the western Mediterranean. In 2026, there are events visible in Mongolia and northern China and in central Mexico, followed by an event visible in 2027 in Thailand, Vietnam, and the Philippines. The uncertainty of these events, even going out to 2027, is good enough to have confidence of the event occurring in these countries, but additional astrometry would be needed to plan observing campaigns.

We were able to find two good non-US occultation opportunities for 2011 HJ_{103}, as shown in Figures 3 and 4. Both are nominally over Central America, with one each in

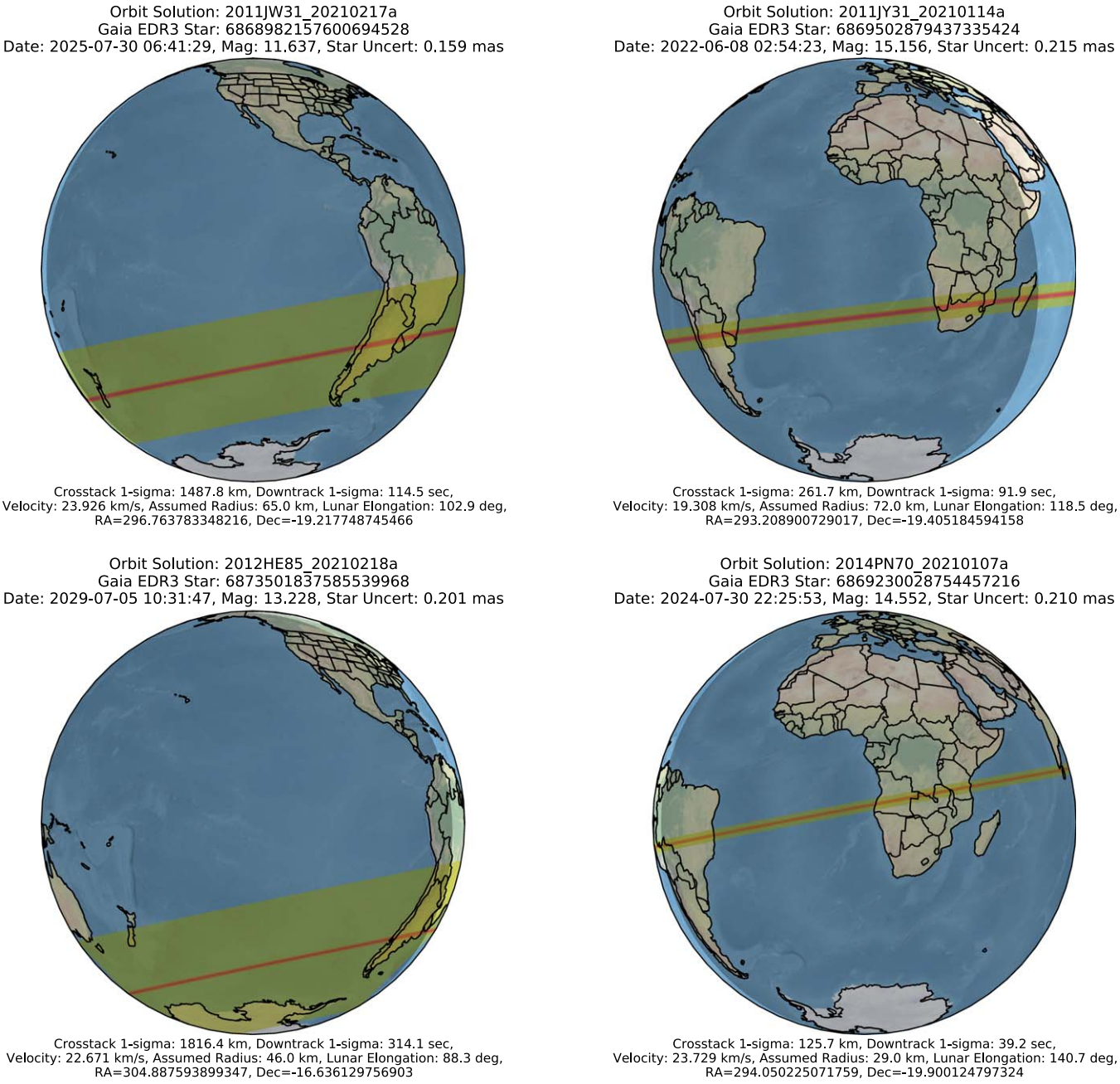

Figure 4. Best international occultation opportunities for 2011 JW_{31}, 2011 JY_{31}, 2012 HE_{85}, and 2014 PN_{70}. The red region represents the nominal shadow path based on the size of the object, and the yellow region adds 1σ uncertainty. Four occultations are shown here; 45 more are available online as a Figure Set.

(The complete figure set (51 images) is available.)

2022 and 2023. The 2023 opportunity is particularly interesting given the star brightness of $G = 13.7$, but additional astrometry, preferably from HST, would be needed to target this event.

We were able to find six good non-US occultation opportunities for 2011 HK_{103}, as shown in Figures 3 and 4. There are two opportunities in 2022 in Chile and Tasmania, one in 2023 in Borneo and Java, two in 2024 in Colombia and Venezuela and in Chile and Argentina, and one in 2027 that crosses India, China, Korea, and Japan. The Chilean events likely have the best prospect for good weather, while the 2027 Asian occultation opportunity could be observed by people in many countries. Object 2011 HK_{103} has a well-defined orbit, so these events are reasonably secure but would need additional astrometry to plan observations, particularly for 2027.

We were able to find three good non-US occultation opportunities for 2011 HZ_{102}, as shown in Figures 3 and 4. The events are in Mongolia in 2023, England in 2025, and southern Africa in 2026. The English occultation event is particularly interesting, as it is the only opportunity that we predicted would be visible from northern Europe.

We were able to find two good non-US occultation opportunities for 2011 JA_{32}, as shown in Figure 4. These are an event in 2025 that nominally passes over Peru and Brazil and an event in 2027 that nominally passes though Central America. However, 2011 JA_{32} has a sufficiently uncertain orbit

that we cannot be confident about these predictions, and additional astrometry of 2011 JA_{32} would be required to even know what country these events are visible in.

We were able to find three good non-US occultation opportunities for 2011 JW_{31}, as shown in Figure 4. These are in Chile and Argentina in 2025 and two events in 2027 that glance South Africa and Australia. The Chile/Argentina occultation is very promising, as the star is very bright at $G = 11.6$. However, the cross-track uncertainty covers the entirety of Chile, and more astrometry of 2011 JW_{31} is absolutely needed.

We were able to find four good non-US occultation opportunities for 2011 JX_{31}, as shown in Figure 4. There are two events in 2023, in New Guinea and in Namibia and Angola, one event in 2024 in southern Africa and Indonesia, and one event in 2029 in southern Chile and Argentina. Object 2011 JX_{31} has a very well-determined orbit, and very little additional astrometry would be needed to observe the 2023 and 2024 events.

We were able to find six good non-US occultation opportunities for 2011 JY_{31}, as shown in Figure 4. There are two events in 2022, first in Brazil and Peru and then in both Argentina and South Africa, followed by an event in Argentina and Brazil in 2023. These events have low nominal uncertainty and would provide a chance to confirm the binary nature of 2011 JY_{31}. There are also 2011 JY_{31} occultations in 2026 in New Zealand and Mongolia and in 2027, where the path crosses much of central Africa, the Arabian Peninsula, Pakistan, and India. The latter two events have very bright stars ($G = 12.7$ and 12.9), and the 2027 event could be observed from a large number of countries.

We were able to find eight good non-US occultation opportunities for 2012 HE_{85}, as shown in Figure 4. These start in 2022 with an event in New Zealand, followed by one that is within 1σ of being observable from Hawaii. In 2023, there is an occultation in Australia and New Guinea, and there is one in East Africa in 2024. There are two occultations in 2025, first over Colombia and Venezuela, and then of a very bright star over much of Africa and Arabia. There is an occultation over Argentina and South Africa in 2026, and in 2029, a $G = 13.2$ star occultation is visible in Chile. Despite all of these opportunities, 2012 HE_{85} still has a relatively uncertain orbit, and more astrometry would absolutely be needed to observe these events.

We were able to find four possible non-US occultation opportunities for 2012 HZ_{84}, as shown in Figure 4. There is one occultation of a very bright star ($G = 12.6$) that nominally passes over South Africa in 2025 and three events in 2027, one in South America and two in Africa. However, 2012 HZ_{84} has a very uncertain orbit and requires more astrometric observations before these events could even be considered for observation.

We were able to find four good non-US occultation opportunities for 2014 PN_{70}, as shown in Figure 4. These events are in 2022 in Africa and Arabia, Canada in 2023, southern Africa in 2024, and Argentina in 2025. Because 2014 PN_{70} has been extensively observed by HST and was observed by New Horizons from a distance of less than 0.1 au, it has an exceptionally high-quality orbit, greatly increasing the plausibility of observing occultations of this relatively small TNO.

We were not able to find any additional international occultation opportunities for 2014 OS_{393} other than the 2023 June 6 event noted above (see Figure 2), which passes over both Mexico and the United States.

We were able to find two good non-US occultation opportunities for 2018 MF_{13}, as shown in Figure 4. One is in 2023 and covers much of Asia, while the second is in 2027 and could be in either North or South America. Object 2018 MF_{13} has a relatively small number of astrometric observations compared to the other TNOs we considered and will very much need more astrometry in the future.

Finally, we were able to find three good non-US occultation opportunities for 2018 MG_{13}, as shown in Figure 4. The first is in 2022 and possibly observable from China, Korea, and Japan. The second 2018 MG_{13} occultation is observable from Chile, and the third is in 2026 and observable from central Africa. Object 2018 MG_{13} has only a 2.5 yr observational arc, so additional astrometry is absolutely needed to know if these events are practical.

5. Summary

We have presented the orbits and occultation opportunities for 15 TNOs that have been observed by the New Horizons spacecraft. Because they have been observed by New Horizons from within the Kuiper Belts, these TNOs have much higher quality heliocentric orbits than most TNOs of similar brightness. We found that 12 of the 15 are consistent with being members of the main Kuiper Belt, two are possibly resonant, and one is a member of the detached-component population. We presented eight possible occultation observation opportunities in 2021–2029 within the United States for these TNOs and 58 more that were observable in other parts of the world. Observation of these occultations would help to provide context to understand the New Horizons flyby target Arrokoth, as well to help calibrate the SFD of the Kuiper Belt.

This work was supported by NASA's New Horizons Kuiper Belt Extended Mission, contract NASW-02008.

Facilities: Magellan:Clay, Magellan:Baade, Subaru, Blanco, HST.

Software: SciPy (Virtanen et al. 2020), emcee package (Foreman-Mackey et al. 2013), HOTPANTS (Becker 2015), spiceypy package (Annex et al. 2020b).

Appendix

The full state vectors and 1σ uncertainty for all 15 objects can be seen in Table 4.

Table 4
State Vectors of the 15 TNOs

TNO	Epoch (ET)	x (km)	y (km)	z (km)	vx (km s^{-1})	vy (km s^{-1})	vz (km s^{-1})
2004 LW_{31}	380,424,492.853	9.6400125506e+08 ±1.02413220e+03	–6.2429724714e+09 ±3.00039573e+04	–2.5282690064e+09 ±1.20967848e+04	4.3548205445e+00 ±4.46760791e-06	9.7770617075e-01 ±1.28093016e-04	1.8891691488e-01 ±5.01455409e-05
2011 HF_{103}	504,048,415.410	1.3374452571e+09 ±9.81581389e+02	–5.8747525328e+09 ±3.95535546e+03	–2.2589004429e+09 ±1.53603689e+03	4.4849364069e+00 ±1.19500449e-05	7.1449206348e-01 ±4.14195635e-05	1.5177674604e-01 ±1.71955329e-05
2011 HJ_{103}	458,248,488.941	1.1678458375e+09 ±3.70479585e+03	–5.5217577728e+09 ±2.01565206e+04	–2.1326728818e+09 ±7.74683653e+03	4.7958608016e+00 ±2.74228505e-05	1.3973019549e+00 ±1.90226351e-04	1.3173287790e-01 ±7.17795909e-05
2011 HK_{103}	506,908,766.065	1.4038625599e+09 ±4.14504118e+02	–5.8483283834e+09 ±1.76470435e+03	–2.2855171898e+09 ±7.10609031e+02	4.3967037040e+00 ±4.74172129e-06	2.2679417736e+00 ±2.16788742e-05	3.8026350727e-01 ±8.12314035e-06
2011 HZ_{102}	477,049,305.283	1.2719707098e+09 ±1.08176397e+03	–5.8834625703e+09 ±7.95877797e+03	–2.3152649281e+09 ±3.16219929e+03	4.4603726309e+00 ±8.54875232e-06	8.3179387718e-01 ±6.64362886e-05	2.3816734164e-01 ±2.56207339e-05
2011 JA_{32}	474,440,278.383	1.2688786214e+09 ±3.88887650e+03	–5.8760956454e+09 ±2.17854685e+04	–2.2670324949e+09 ±8.20816168e+03	4.4965082527e+00 ±2.99956203e-05	1.2503461232e+00 ±1.84760908e-04	7.2112682230e-01 ±7.69035017e-05
2011 JW_{31}	472,873,300.212	1.2416993511e+09 ±1.40416710e+03	–5.8357355980e+09 ±6.13038927e+03	–2.3133041551e+09 ±2.29885472e+03	4.5259857409e+00 ±1.06397940e-05	1.1315654882e+00 ±4.88493811e-05	5.2993072587e-01 ±1.75348335e-05
2011 JX_{31}	552,712,928.489	1.6120707866e+09 ±6.77241304e+02	–6.4162653916e+09 ±4.55603303e+03	–2.5200920200e+09 ±1.82474333e+03	4.1769572787e+00 ±9.70415565e-06	5.7357008728e-01 ±4.87785717e-05	5.0166048603e-02 ±1.85615097e-05
2011 JY_{31}	473,881,748.705	1.2385640713e+09 ±8.56816097e+02	–5.8198221788e+09 ±6.39470238e+03	–2.2820608943e+09 ±2.49054004e+03	4.4979532372e+00 ±7.22979952e-06	9.8060375543e-01 ±5.48455680e-05	5.6463277507e-01 ±2.20824890e-05
2012 HE_{85}	476,917,176.604	1.2150208288e+09 ±1.06164230e+03	–5.4909130806e+09 ±4.39785596e+03	–2.1296591618e+09 ±1.81455763e+03	4.8306693628e+00 ±1.14439535e-05	7.8354090659e-01 ±4.85618408e-05	5.3734651420e-01 ±2.18921531e-05
2012 HZ_{84}	461,543,007.271	1.157,138,001,1e+09 ±2.87339492e+03	–5.5844059679e+09 ±1.60349549e+04	–2.1651851823e+09 ±6.07785622e+03	4.6034465164e+00 ±2.63548188e-05	1.4028021041e+00 ±1.50301493e-04	1.0355626413e+00 ±6.45071194e-05
2014 OS_{393}	478,780,631.678	1.2771862964e+09 ±7.41039429e+02	–5.9228394979e+09 ±3.78315890e+03	–2.2859712865e+09 ±1.45745034e+03	4.4826807549e+00 ±5.84980655e-06	8.8293470147e-01 ±3.13301507e-05	1.2030011947e-01 ±1.22129063e-05
2014 PN_{70}	599,572,896.684	1.7999492868e+09 ±3.68319720e+01	–5.8842594246e+09 ±1.76272562e+02	–2.2907531400e+09 ±4.82880287e+01	4.2564962371e+00 ±4.74238884e-06	1.4723295157e+00 ±2.40790148e-05	3.2406068796e-01 ±9.66128099e-06
2018 MF_{13}	599,572,896.684	2.0132043990e+09 ±1.06887053e+03	–5.9723152487e+09 ±3.03495773e+03	–2.6334983188e+09 ±2.33275319e+03	3.6039270433e+00 ±1.41941997e-05	1.9827207355e+00 ±1.54026030e-04	6.2400919602e-01 ±6.44724078e-05
2018 MG_{13}	599,572,896.684	2.0135678524e+09 ±5.24285536e+03	–6.2148688590e+09 ±1.52750756e+04	–2.3975561653e+09 ±5.75300975e+03	4.0919909806e+00 ±1.36410035e-04	1.6967762278e+00 ±5.15685497e-04	–9.6606741470e-02 ±1.97640606e-04

Note. The epoch for each state vector is in JPL ET, seconds of TDB elapsed since the J2000.0 epoch (see text). The state vectors are in the ICRF frame and relative to the solar system barycenter. Units are kilometers and seconds to allow the easiest interface with JPL SPICE and related tools.

ORCID iDs

Simon B. Porter https://orcid.org/0000-0003-0333-6055
Anne Verbiscer https://orcid.org/0000-0002-3323-9304
Susan Benecchi https://orcid.org/0000-0001-8821-5927
H. A. Weaver https://orcid.org/0000-0003-0951-7762
Hsing Wen Lin https://orcid.org/0000-0001-7737-6784
J. J. Kavelaars https://orcid.org/0000-0001-7032-5255
Wesley C. Fraser https://orcid.org/0000-0001-6680-6558
David W. Gerdes https://orcid.org/0000-0001-6942-2736
Marc W. Buie https://orcid.org/0000-0003-0854-745X
Kelsi N. Singer https://orcid.org/0000-0003-3045-8445
Joel W. Parker https://orcid.org/0000-0002-3672-0603
S. Alan Stern https://orcid.org/0000-0001-5018-7537

References

Alard, C., & Lupton, R. H. 1998, ApJ, 503, 325
Altamimi, Z., Rebischung, P., Métivier, L., & Collilieux, X. 2016, JGRB, 121, 6109
Annex, A., Pearson, B., Seignovert, B., et al. 2020a, JOSS, 5, 2050
Annex, A. M., Pearson, B., Seignovert, B., et al. 2020b, JOSS, 5, 2050
Astropy Collaboration, Robitaille, T. P., Tollerud, E. J., et al. 2013, A&A, 558, A33
Bannister, M. T., Gladman, B. J., Kavelaars, J. J., et al. 2018, ApJS, 236, 18
Becker, A. 2015, HOTPANTS: High Order Transform of PSF ANd Template Subtraction, Astrophysics Source Code Library, ascl:1504.004
Benecchi, S., Parker, A., Porter, S., et al. 2020, AAS/Division for Planetary Sciences Meeting Abstracts, 52, 307.02
Benecchi, S. D., Borncamp, D., Parker, A. H., et al. 2019, Icar, 334, 22
Benecchi, S. D., & Sheppard, S. S. 2013, AJ, 145, 124
Bigelow, B. C., Dressler, A. M., Shectman, S. A., & Epps, H. W. 1998, Proc. SPIE, 3355, 225
Brankin, R. W., Gladwell, I., Dormand, J. R., Prince, P. J., & Seward, W. L. 1989, ACM Trans. Math. Softw., 15, 31
Buie, M. W., Porter, S. B., Tamblyn, P., et al. 2020, AJ, 159, 130
Calabretta, M. R., & Greisen, E. W. 2002, A&A, 395, 1077
Cheng, A. F., Weaver, H. A., Conard, S. J., et al. 2008, SSRv, 140, 189
Dotto, E., Perna, D., Barucci, M. A., et al. 2008, A&A, 490, 829
Elliot, J. L., Kern, S. D., Clancy, K. B., et al. 2005, AJ, 129, 1117
Elliot, J. L., Person, M. J., Zuluaga, C. A., et al. 2010, Natur, 465, 897
Flaugher, B., Diehl, H. T., Honscheid, K., et al. 2015, AJ, 150, 150
Folkner, W. M., Williams, J. G., Boggs, D. H., Park, R. S., & Kuchynka, P. 2014, IPNPR, 42, 1
Foreman-Mackey, D., Hogg, D. W., Lang, D., & Goodman, J. 2013, PASP, 125, 306
Fraser, W. C., Brown, M. E., Morbidelli, A., Parker, A., & Batygin, K. 2014, ApJ, 782, 100
Gaia Collaboration, Brown, A. G. A., Vallenari, A., et al. 2018, A&A, 616, A1
Ginsburg, A., Sipőcz, B. M., Brasseur, C. E., et al. 2019, AJ, 157, 98
Greisen, E. W., & Calabretta, M. R. 2002, A&A, 395, 1061
Grundy, W. M., Noll, K. S., Roe, H. G., et al. 2019, Icar, 334, 62
Gwyn, S. D. J., Hill, N., & Kavelaars, J. J. 2012, PASP, 124, 579
Hofgartner, J. D., Buratti, B. J., Benecchi, S. D., et al. 2021, Icar, 356, 113723
Kimble, R. A., MacKenty, J. W., O'Connell, R. W., & Townsend, J. A. 2008, Proc. SPIE, 7010, 70101E
Krist, J. E., Hook, R. N., & Stoehr, F. 2011, Proc. SPIE, 8127, 81270J
Lang, D., Hogg, D. W., Mierle, K., Blanton, M., & Roweis, S. 2010, AJ, 139, 1782
Leiva, R., Buie, M. W., Keller, J. M., et al. 2020, PSJ, 1, 48
Levison, H. F., Morbidelli, A., Van Laerhoven, C., Gomes, R., & Tsiganis, K. 2008, Icar, 196, 258
Lindegren, L., Klioner, S. A., Hernández, J., et al. 2021, A&A, 649, A2
Ma, C., Arias, E. F., Bianco, G., et al. 2009, ITN, 35, 1
Ma, C., Arias, E. F., Eubanks, T. M., et al. 1998, AJ, 116, 516
Magnier, E. A., Schlafly, E., Finkbeiner, D., et al. 2013, ApJS, 205, 20
Malhotra, R. 1993, Natur, 365, 819
McKinnon, W. B., Richardson, D. C., Marohnic, J. C., et al. 2020, Sci, 367, aay6620
McLeod, B., Geary, J., Conroy, M., et al. 2015, PASP, 127, 366
Miyazaki, S., Komiyama, Y., Nakaya, H., et al. 2012, Proc. SPIE, 8446, 84460Z
Nelder, J. A., & Mead, R. 1965, CompJ, 7, 308
Nesvorný, D., & Vokrouhlický, D. 2019, Icar, 331, 49
Nesvorný, D., Youdin, A. N., & Richardson, D. C. 2010, AJ, 140, 785
Ortiz, J. L., Santos-Sanz, P., Sicardy, B., et al. 2017, Natur, 550, 219
Ortiz, J. L., Sicardy, B., Braga-Ribas, F., et al. 2012, Natur, 491, 566
Pence, W. D., Chiappetti, L., Page, C. G., Shaw, R. A., & Stobie, E. 2010, A&A, 524, A42
Person, M. J., Bosh, A. S., Zuluaga, C. A., et al. 2021, Icar, 356, 113572
Porter, S. B., Buie, M. W., Parker, A. H., et al. 2018, AJ, 156, 20
Porter, S. B., Spencer, J. R., Benecchi, S., et al. 2016, ApJL, 828, L15
Santos-Sanz, P., Lellouch, E., Fornasier, S., et al. 2012, A&A, 541, A92
Sicardy, B., Ortiz, J. L., Assafin, M., et al. 2011, Natur, 478, 493
Spencer, J. R., Stern, S. A., Moore, J. M., et al. 2020, Sci, 367, aay3999
Stern, S. A., Weaver, H. A., Spencer, J. R., et al. 2019, Sci, 364, aaw9771
Stetson, P. B. 1987, PASP, 99, 191
Tchebychev, P. 1853, Théorie des mécanismes connus sous le nom de parallélogrammes (St. Petersburg: Imprimerie de l'Académie impériale des sciences)
Thirouin, A., & Sheppard, S. S. 2018, AJ, 155, 248
Thirouin, A., & Sheppard, S. S. 2019, AJ, 157, 228
Valdes, F., & Gruendl, R. 2014, in ASP Conf. Ser. 485, Astronomical Data Analysis Software and Systems XXIII, ed. N. Manset & P. Forshay (San Francisco, CA: ASP), 379
Verbiscer, A. J., Porter, S., Benecchi, S. D., et al. 2019, AJ, 158, 123
Vera C. Rubin Observatory LSST Solar System Science Collaboration, Jones, R. L., Bannister, M. T., et al. 2020, arXiv:2009.07653
Virtanen, P., Gommers, R., Oliphant, T. E., et al. 2020, NatMe, 17, 261
Weaver, H. A., Cheng, A. F., Morgan, F., et al. 2020, PASP, 132, 035003
Weaver, H. A., Porter, S. B., Spencer, J. R. & The New Horizons Science Team 2022, PSJ, in press